4 Results & Discussion

4.1 Rational behind the design of FA hybrid analogs

To improve the cholinesterase inhibition, antioxidant activity, and metal chelation ability of the compound **EJMC-4e** [147], a series of rationally designed structural modifications was developed. The study initially investigated the impact of linker length by introducing spacers between left-side FA moiety and right-side amine with diverse sizes. After optimization of the linker length, the effect of the Michael acceptor concept on the inhibition of cholinesterase was subsequently assessed by replacing FA with 3-(4-hydroxy-3methoyphenyl)propanoic acid. Furthermore, the impact of hydroxy and methoxy groups located on the phenyl ring of FA on enzyme inhibition activity was examined. The results highlighted the critical role played by the double bond, methoxy, and hydroxy groups on enzyme inhibition properties, leading to the decision to keep the FA fragment constant while introducing modifications on the other side of the molecule. As phenols are renowned for their radical scavenging properties, incorporating the hydroxyl group in various positions of the phenyl ring was carried out [161, 162]. The evaluation of these modifications aimed to determine whether they would also contribute to improved anticholinesterase activities. The pyridine moiety is well-documented for its anticholinesterase properties and metal chelation capabilities [4, 163]. So, we replaced the m-anisidine with pyridine moieties into **EJMC-4e (Figure 4.1)** to determine its impact on AChE/BChE inhibitory activity. In addition to the pyridine moiety, we explored incorporating biphenyl and naphthyl rings to enhance the developed compound's anticholinesterase activity.

Based on our earlier observation of the well-tolerated behavior of quinoline moiety against AChE/BChE, we replaced m-anisidine in **EJMC-4e** with quinoline moiety and evaluated its effect on enzyme activities. Notably, the selection of the 8-hydroxyquinoline moiety for further

exploration was driven by its well-established role in metal chelation and modulation of Aβ, as extensively documented in the literature [164-166]. Therefore, it was deemed a promising pharmacophore for developing potential AD agents. Building upon this rationale, we introduced the 8-hydroxyquinoline moiety to explore its impact on the enzyme inhibition activities. We aim to advance our understanding of the optimal structural features required for enhanced anticholinesterase activity, antioxidant properties, Aβ aggregation, and metal chelation activity. We also evaluated the lead-identified molecule in *in-vitro* and *in-vivo* models. This comprehensive iterative approach allows for the systematic optimization of **EJMC-4e** by elucidating the structural features that enhance cholinesterase inhibition, antioxidant activity, metal chelation, and other multifunctional properties.

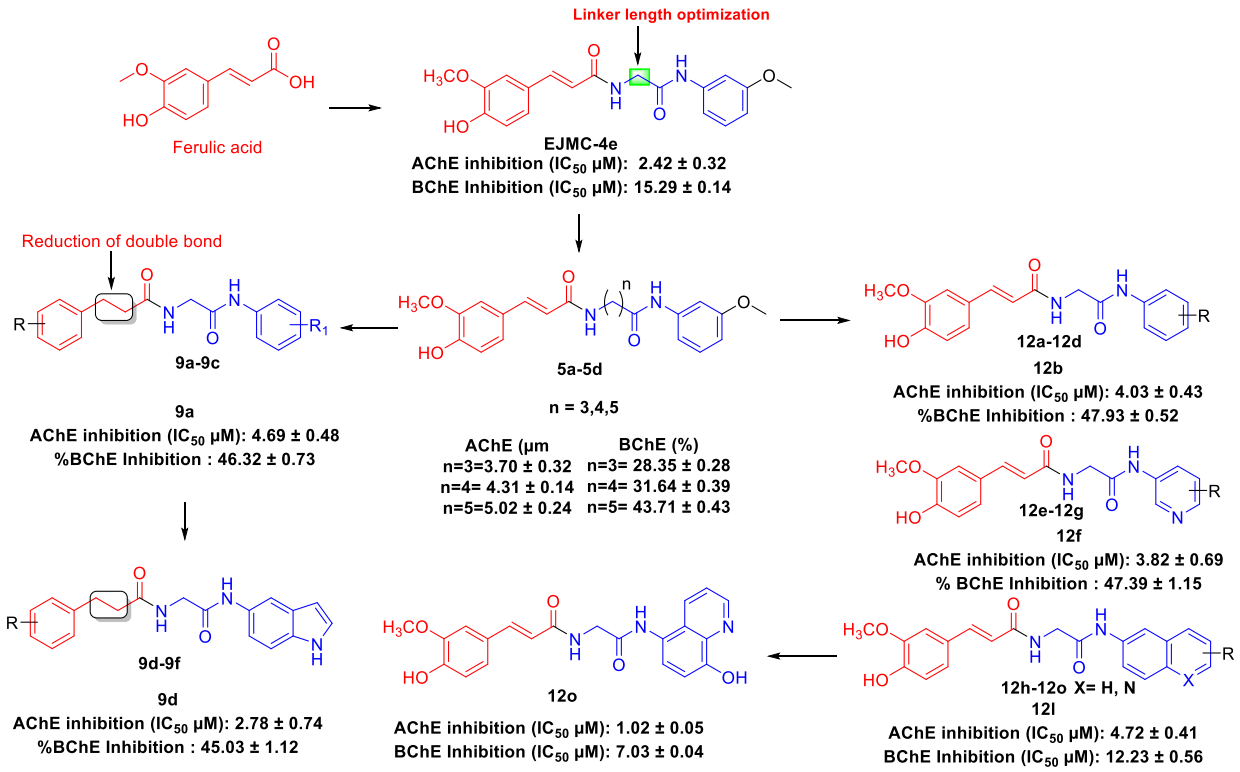

Figure 4.1: The design strategies of novel multifunctional naturally inspired ferulic acid derivatives.

4.2 Chemistry involved in the first series (novel ferulic acid) derivatives

The reactions involved for novel FA derivatives are presented in schemes 1-3. The amino acids of varying lengths (3-5 linker) were treated with boc-anhydride to obtain the desired boc-protected amino acids **(2a-2c)**; after that, these intermediates were treated with m-anisidine to perform a coupling reaction to yield intermediates **(3a-3c)** [167] followed by the treatment with TFA to get the desired intermediate **(4a-4c)**. Finally, the target compounds **5a-5c** were synthesized by the reaction of intermediates **4a-c** with FA under the standard amide coupling conditions [150].

In scheme **2**, the commercially available substituted amines were treated with chloroacetylchloride to get intermediates **7a-7b** and then treated with an excess of aqueous ammonia to obtain intermediates **8a-8b** following our earlier publications [147]. The target compounds **9a-9f** were synthesized by treating **8a-8b** with different substituted acids in the presence of EDCI, HOBt, and TEA under a nitrogen environment.

In scheme **3,** the intermediates **10a-10o** were synthesized by treating commercially available substituted amines with chloroacetylchloride in the presence of triethylamine following earlier publications[147, 150]. These intermediates further reacted with excess aqueous ammonia to yield intermediates **11a-11o**. The synthesis of target compounds **12a-12o** was carried out by utilizing intermediates **11a-11o**, which were treated with FA in the presence of EDC—HCl, HOBt, and triethylamine.

4.3 Biological evaluation of the first series (novel ferulic acid) derivatives

4.3.1 *In-vitro* inhibition studies of *h*AChE and *eq*BChE

We selected **EJMC-4e** from our previous research work as a starting point in the present study. Initially, we investigated the effect of increasing the linker length between the FA and aniline

moieties in the parent molecule**, EJMC-4e**. Our earlier publication reported a compound with spacer having two atoms [150]. Hence, compounds **5a-5c** with different spacer lengths were synthesized and evaluated for their anticholinesterase activity. Compounds **5a-5c** with spacers having 3-5 atoms were turn out to be slightly weak inhibitors of AChE (IC_{50}, (μM) AChE, **5a** = 3.70 ± 0.32, **5b** = 4.31 ± 0.14 and **5c** = 5.02 ± 0.24, respectively), and drastic reduction in the inhibitory activity against BChE (% inhibition BChE at 20 μM, **5a** = 28.35 ± 0.28, **5b** = 31.64 ± 0.39, and **5c** = 43.71 ± 0.43 respectively) over **EJMC-4e** IC_{50}, (μM) AChE, 2.42 ± 0.32, and IC_{50}, (μM) BChE, 15.29 ± 0.14. These findings revealed that the linker length does not positively impact anticholinesterase activity; therefore, we decided to proceed with a single spacer. Next, we investigated the impact of the double bond present in FA on cholinesterase activity. We started with 3-(4-hydroxy-3-methoxyphenyl)propanoic acid, resulting in the synthesis of compound **9a**, which exhibited significantly decreased activity against AChE with IC_{50}, (μM), 4.69 ± 0.48 and % inhibition for BChE at 20 μM, 46.32 ± 0.73 compared to **EJMC-4e**. Furthermore, we explored the effects of the hydroxyl and methoxy functional groups on the phenyl ring of the FA portion on the enzyme inhibition property, which resulted in the development of **9b** and **9c**. These modifications also resulted in approximately 50% reduction in activity against AChE enzyme with IC_{50}, (μM) AChE, **9b** = 8.93 ± 0.34 and **9c** = 7.67 ± 0.09, respectively) compared to compound **9a** (IC_{50}, (μM) AChE, 4.69 ± 0.48). Similarly, BChE inhibition property slightly reduced in the newly synthesized molecules (% inhibition at 20 μM, 43.71 ± 0.62 for compound **9b** and 39.56 ± 1.05 for compound **9c**), compared to **9a** (% inhibition at 20 μM, 46.32 ± 0.73). These findings indicated the necessity of a double bond, the methoxy and hydroxy groups, for retaining the enzyme inhibition activity.

Based on our earlier reports, we replaced the phenyl ring located on the distal portion of **EJMC-4e** with an indole ring to develop **9d-9f**. A significant reduction in the enzyme inhibition activity was observed (IC_{50}, (μM) AChE, **9d** = 2.78 ± 0.74, **9e** = 4.80 ± 0.42, and **9f** = 3.53 ± 0.59, and BChE % inhibition at 20 μM, **9d** = 45.03 ± 1.12, **9e** = 37.98 ± 0.83, and **9f** = 41.07 ± 0.76, respectively) compared to compound **EJMC-4e (**IC_{50}, (μM) AChE, 2.42 ± 0.32, and IC_{50} (μM) BChE, 15.29 ± 0.14.). These results further confirmed the importance of the double bond, methoxy, and hydroxy groups in maintaining enzyme inhibitory activity. Hence, it is evident from our results that structural modifications on FA moiety are not well tolerated in terms of the enzyme inhibition property.

Next, we replaced the 3-methoxy group on the phenyl ring of the aniline portion of **EJMC-4e** with a hydroxy group on different positions of the aniline ring, resulting in the development of compounds **12a-c**. Intriguingly, none of the synthesized derivatives demonstrated potency surpassing that of **EJMC-4e** (IC_{50}, (μM) AChE **12a** = 5.39±0.61, **12b** = 4.03 ± 0.43, **12c** = 4.10 ± 0.28 and BChE % inhibition at 20 μM, **12a** = 45.98 ± 0.43, **12b** = 47.93 ± 0.52 and **12c** = 37.91 ± 0.74, respectively). Subsequently, we replaced the phenyl ring with a biphenyl ring, leading to the synthesis of compound **12d** (IC_{50}, (μM), AChE, **12d** = 3.57 ± 0.47, and BChE % inhibition at 20 μM, 45.98 ± 0.29, respectively). Next, replacement of the aniline moiety of **EJMC-4e** with pyridine resulted in the synthesis of **12e-12g**. These compounds expressed moderate anticholinesterase activity with IC_{50}, (μM), AChE, **12e** = 4.15 ± 0.53, **12f** = 3.82 ± 0.69, and **12g** = 4.96 ± 0.36, and BChE % inhibition at 20 μM, **12e** = 39.15 ± 0.84, **12f** = 47.39 ± 1.15, and **12g** 43.74 ± 0.46, respectively. Next, we replaced the phenyl ring present on the right side of compound **EJMC-4e** with a naphthyl ring to yield **12h** having IC_{50}, (μM), AChE, 7.39±0.40 and IC_{50}, (μM), BChE, 10.10±0.71, respectively. After that, we decided to explore

the different positions of quinoline and replaced the phenyl ring of **EJMC-4e** with different positioned quinoline rings to develop **12i-12n** and evaluate their anticholinesterase activity. Among all quinoline synthesized derivatives, **12l** (5^{th} position of quinoline) derivative showed a balance AChE and BChE activity with IC_{50}, (μM) AChE, 4.72 ± 0.41 and IC_{50}, (μM) BChE, 12.23 ± 0.56, respectively. The other quinoline derivatives demonstrate moderate enzyme inhibition activity with IC_{50}, (μM) or % inhibition against AChE, **12i** = 4.28 ± 0.26 μM, **12j** = 46.35 ± 0.03%, **12k** = 5.97 ± 0.71 μM, **12m** = 4.44 ± 0.72 μM, and **12n** = 48.95 ± 0.63 %, respectively and BChE % inhibition at 20 μM, **12i** = 44.89 ± 0.63, **12j** = 42.83 ± 1.09, **12k** = 47.93 ± 0.92, **12m** = 43.74 ± 0.31, and **12n** = 39.37 ± 0.46, respectively (**table 1**). The findings of these studies revealed that the 3^{rd} position of quinoline is less favorable for anticholinesterase activity. Further, we introduced 8-hydroxyquinoline given its metal-chelating and Aβ-modulating effects to synthesize **12o**. To our advantage, **12o** was found to be the most potent inhibitor among all synthesized molecules with IC_{50}, (μM), AChE, 1.02 ± 0.05 and IC_{50}, (μM), BChE, 7.03 ± 0.04. Therefore, we selected **12o** for further *in-vitro* and *ex-vivo* evaluation.

Table 4.1: Cholinesterase inhibitory activities of the developed derivatives.

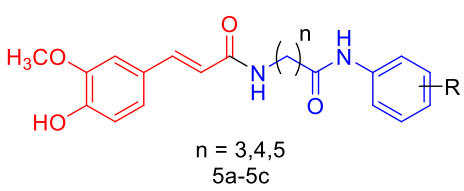

n = 3,4,5
5a-5c

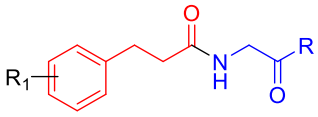

9a-9f

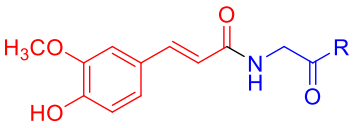

12a-12o

S.No.	R	*h*AChE IC_{50}, (μM)	*eq*BChE(% inhibition)
5a	m-methoxy	3.70 ± 0.32	28.35 ± 0.28
5b	m-methoxy	4.31 ± 0.14	31.64 ± 0.39
5c	m-methoxy	5.02 ± 0.24	43.71 ± 0.43
9a	m-anisidine	4.69 ± 0.48	46.32 ± 0.73
9b	m-anisidine	8.93 ± 0.34	43.71 ± 0.62
9c	m-anisidine	7.67 ± 0.09	39.56 ± 1.05
9d	5-aminoindole	2.78 ± 0.74	45.03 ± 1.12
9e	5-aminoindole	4.80 ± 0.42	37.98 ± 0.83
9f	5-aminoindole	3.53 ± 0.59	41.07 ± 0.76
12a	o-aminophenol	5.39 ± 0.61	45.98 ± 0.43
12b	m-aminophenol	4.03 ± 0.43	47.93 ± 0.52
12c	p-aminophenol	4.10 ± 0.28	37.91 ± 0.74
12d	biphenylamine	3.57 ± 0.47	45.98 ± 0.29
12e	o-aminopyridine	4.15 ± 0.53	39.15 ± 0.84
12f	m-aminopyridine	3.82 ± 0.69	47.39 ± 1.15
12g	p-aminopyridine	4.96 ± 0.36	43.74 ± 0.46

12h	napthylamine	7.39 ± 0.40	10.10 ± 0.71 µM
12i	2-aminoquinoline	4.28 ± 0.26	44.89 ± 0.63
12j	3-aminoqunoline	46.35 ± 0.03%	42.83 ± 1.09
12k	4-aminoqunoline	5.97 ± 0.71	47.93 ± 0.92
12l	5-aminoqunoline	4.72 ± 0.41	12.23 ± 0.56 µM
12m	6-aminoqunoline	4.44 ± 0.72	43.74 ± 0.31
12n	7-aminoqunoline	48.95 ± 0.63 %	39.37 ± 0.46
12o	8-amino-5-hdroxy-quinoline	1.02 ± 0.05	7.03 ± 0.04 µM

IC_{50} = 50% inhibitory concentration (means ± SD of 3 independent experiments)

% Inhibition was determined at 20μM inhibitor concentration (in triplicate)

4.3.2 Enzyme kinetics studies with compound 12o

The study of enzyme inhibition is facilitated by applying enzyme kinetics, a valuable investigative approach for understanding the underlying mechanisms. For this experiment, **12o**, which exhibited the highest inhibitory activity against ChEs among the developed molecules, was chosen to investigate its mechanism of inhibition. The Lineweaver-Burk reciprocal plot (**Figure 4.2)** is a widely employed technique for analyzing enzyme kinetics data. The procedure entails graphing the reciprocal of the velocity of the initial enzyme reaction (1/V) against the reciprocal of the substrate concentration (1/[S]). The experimental data demonstrated that **12o** exhibited a mixed-type inhibition against both *h*AChE and *eq*BChE. This type of inhibition manifests when the inhibitor can bind to both the enzyme and the enzyme-substrate complex, reducing the reaction rate. The precise mechanism of mixed-type

inhibition may exhibit variability contingent upon the particular enzyme and inhibitor under consideration. This experiment offers valuable insights into how compound **12o** inhibits cholinesterases (ChEs). These findings can potentially inform the development of enhanced ChE inhibitors for treating neurological disorders.

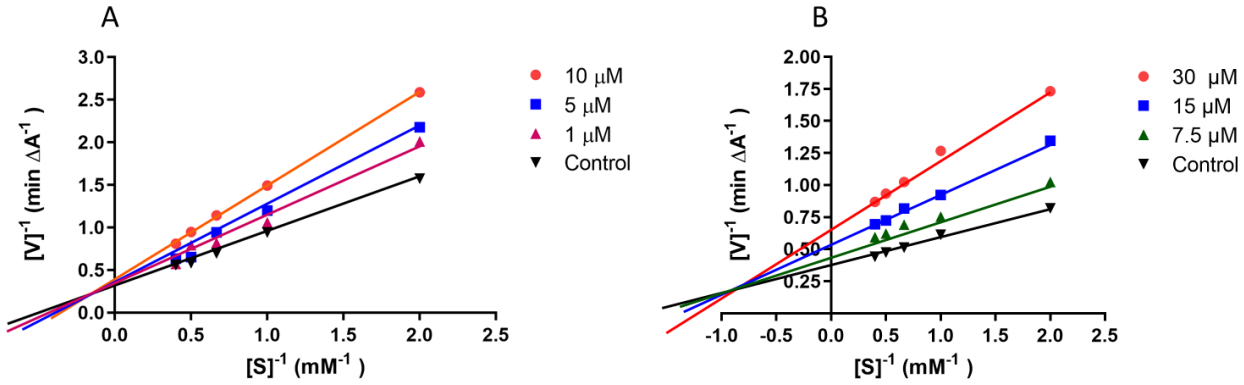

Figure 4.2: A kinetics study to investigate the mechanism of ChE inhibition by compound **12o**. A) Lineweaver-Burk reciprocal plots based on *h*AChE initial velocity were overlaid, showing the effects of increasing substrate concentration (ranging from 0.5 to 3.0 mM) in the absence or presence of **12o** at 1, 5, and 10 µM. Here, [S] represents the concentration of acetylthiocholine, and [V] represents the initial velocity rate. B) Lineweaver-Burk reciprocal plots for *eq*BChE initial velocity with increasing substrate concentration (5, 10, 15, 20, and 25 mM) in the absence or presence of 12 at 7.5, 15, and 30 mM concentrations. In this case, [S] represents the concentration of butyrylthiocholine, and [V] represents the initial velocity rate. The lines on the plots were generated through a weighted least-squares analysis of the data points. The reported experimental data represent two independent experiments means ± standard deviation.

4.3.3 In-silico study with lead compound 12o

4.3.3.1 Molecular docking studies with 12o

Compound **12o** exhibited well-balanced activity against both AChE and BChE in *in-vitro* studies. Therefore, we selected **12o**, **EJMC-4e**, and **DPZ** for molecular docking studies against AChE (4EY7) and BChE (4BDS). Molecular modeling revealed that **12o** exhibits key interactions with AChE (PDB # 4EY7), including π-alkyl interaction with Trp286 and hydrogen bonding with Ser293, Tyr124, Ser203, and Gly121. It also engaged in π-cation and π-π interactions with His447 and Trp86 (**Figure. 4.3**). The **EJMC-4e** forms hydrogen bonds with Tyr133 and Tyr124, along with engaging in π-π and π-alkyl interactions with Trp286 and Trp86, and van der Waals interactions with Val294 (**Figure 4.3 C**). In contrast, **DPZ** demonstrates π-π stacked interactions with Tyr341 and Trp86, hydrogen bonding with Tyr124, π-sigma interaction with Trp286, and π-alkyl interactions with Phe338, Tyr337, Leu289, and Tyr72 (**Figure 4.3 E**). **12o** shares a few everyday interactions with standard **DPZ**. The binding energies for **12o**, **EJMC-4e**, and **DPZ** were observed as -11.5 kcal/mol, -10.0 kcal/mol, and -11.7 kcal/mol, respectively. These findings suggest that **12o** exhibits a higher binding affinity than **EJMC-4e** and is almost comparable to the standard **DPZ**. **12o** formed conventional hydrogen bonds with Gly116 and Ser198, π-π stacking with Phe329, π-alkyl interactions with Val288, Leu286, and Val331 π-lone with Ala328 and π -donor hydrogen bond with Trp231, and His 438 (**Figure. 4.3 B**) against BChE (PDB # 4BDS). Additionally, **EJMC-4e** demonstrated hydrogen bond interactions with Trp82, Trp430, Gly117, π-sigma interactions with Ala328, π-π interactions with Phe329, and π-alkyl interactions with Leu286 (**Figure 4.3 D**). On the other hand, **DPZ** established hydrogen bonds with Thr120, π-sigma interactions with Trp82, π-π interactions with Trp23, and π-alkyl interactions with His438, Met437, Trp430, Ala328, and hydrogen bond interaction with Pro285, Glu197 and Gly116 (**Figure.**

4.3F). The binding affinities of **12o**, **EJMC-4e**, and **DPZ** against 4BDS were determined to be -9.3 kcal/mol, -8.8 kcal/mol, and -9.8 kcal/mol, respectively. Despite unfavorable interactions in **12o** leading to reduced binding affinity, it still exhibits a higher binding affinity than **EJMC-4e**. Molecular docking results concurred with *in-vitro* findings, elucidating **12o**'s balanced activity through specific active site interactions.

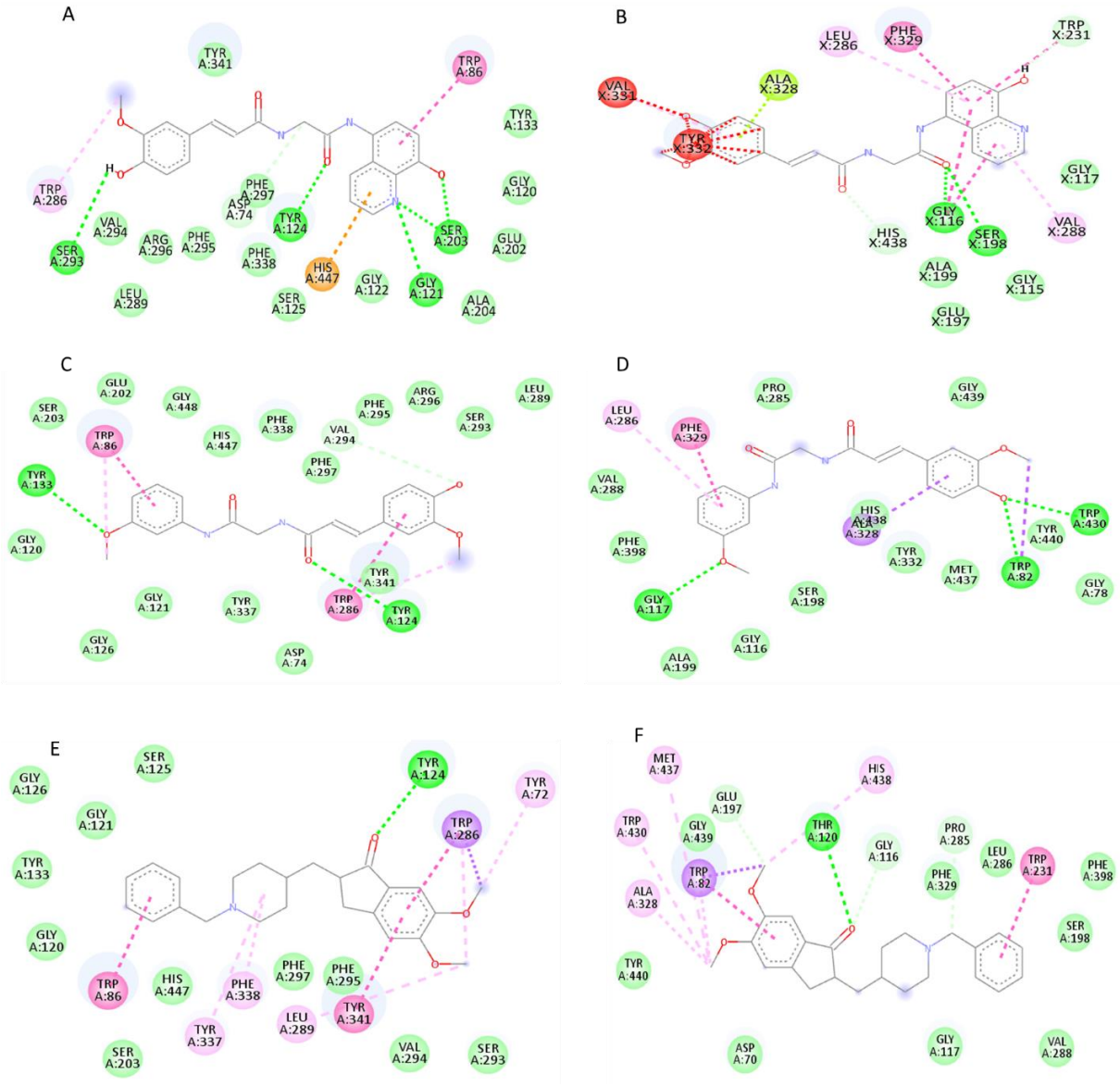

Figure 4.3: Molecular docking study of **12o** against AChE and BChE. A) 2d interaction diagram of **12o** against 4EY7. B) 2d interaction diagram of **12o** against 4BDS. C)) 2d

interaction diagram of **EJMC-4e** against 4EY7. D) 2d interaction diagram of **12o** against 4BDS. E) 2d interaction diagram of **DPZ** against 4EY7. F)) 2d interaction diagram of **DPZ** against 4BDS.

4.3.3.2 Molecular dynamics studies with lead molecule 12o

After initial docking analysis, the binding mode predictions for compound **12o** with proteins were assessed using molecular dynamics simulations. This aimed to enhance understanding of interactions, conformational changes, and stability during a 100 ns simulation. Root mean square deviation (RMSD) tracked the system's stability, with RMSD < 0.25 nm indicating proximity to the reference structure. The protein 4EY7 exhibits stable configuration against **12o**, **EJMC-4e**, and **DPZ** with RMSD values in the range of 0.15-0.28 nm, 0.14-0.28 nm, and 0.14-0.28 nm, respectively (**Figure 4.4 A**). Similarly, 4BDS protein showed stability throughout the simulation against **12o**, **EJMC-4e**, and **DPZ** with RMSD values in the range 0.17-0.32 nm, 0.12-0.29 nm, and 0.12-0.28 nm, respectively (**Figure 4.5 A**). The RMSD value of ligand **12o**, **EJMC-4e**, and **DPZ** against 4EY7 was found to be in the range of 0.17-0.50 nm, 0.09-0.43, and 0.35-1.75 nm (**Figure 4.4 B**) respectively. The RMSD data showed that our lead **12o** exhibited better stability against 4EY7 protein than **EJMC-4e** and **DPZ**. Similarly, **12o, EJMC-4e, and DPZ** showed RMSD values in the range of 0.15-0.6 nm, 0.06-0.68 nm, and 0.10- 5.98 nm (**Figure 4.5 B**) against 4BDS protein which suggests that **12o** showed the most deviation in the initial time of the simulation and the acquire a stable configuration throughout the simulation up to 100 ns compared to **EJMC-4e** and **DPZ**. This result mimics the outcome from *in-vitro* enzyme activity, where the compound showed less activity against BChE than AChE.

Analysis of root-mean-square fluctuations (RMSFs) explored amino acid residue variability during simulation. RMSFs for 4EY7 against **12o**, **EJMC-4e**, and **DPZ** were 0.5-0.70 nm (**Figure 4.4 C**). The 4BDS protein shows RMSF against **12o** and **EJMC-4e** in the range of approximately 0.05-0.48 nm, respectively, whereas the 4BDs protein exhibits RMSF value in the 0.5-0.7 nm (**Figure 4.5 C**) against **DPZ**. The higher flexibility was observed in the C- and N-termini due to solvent exposure. Compounds **12o**, **EJMC-4e**, and **DPZ** showed narrower fluctuations against 4EY7 in the range 0.02-0.13 nm, 0.03-0.20 nm and 0.5-0.28 nm (**Figure 4.4 D**), respectively than 4BDS with RMSF value in the range 0.03-0.25 nm, 0.04-0.32 nm and 0.06-0.28nm (**Figure 4.5 D**) respectively, suggesting more effective binding of ligands against 4EY7 compared to 4BDS. The result indicates that **12o** showed a narrow fluctuation against 4EY7 compared to **EJMC-4e** and **DPZ**. Compounds **12o**, **EJMC-4e** and **DPZ** show a radius of gyration value in the range of 0.28-2.35 nm, 0.27-2.31 nm and 0.28-2.32 (**Figure 4.4 E**) against 4EY7 and 2.31-2.36 nm, 2.28-2.32 nm and 2.28-2.35 nm (**Figure 4.5 E**) against 4BDS respectively. This observation suggests that the system effectively maintains its three-dimensional quaternary geometrical proportions without experiencing any sudden expansion during the simulation period.

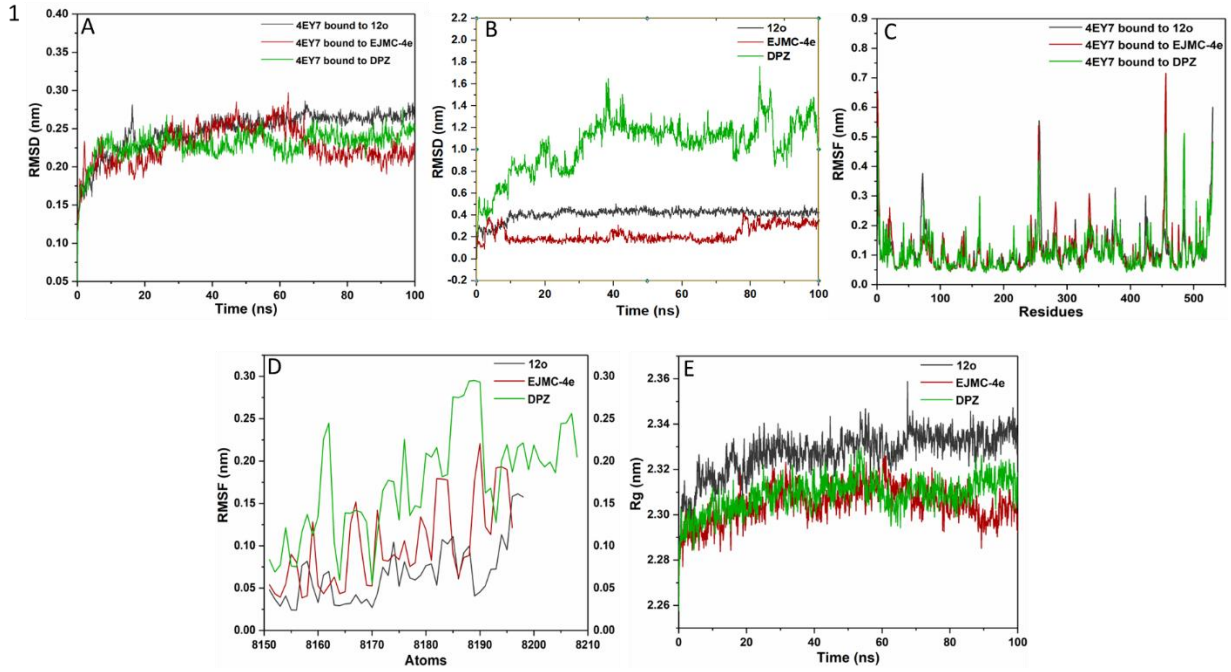

Figure 4.4: Molecular dynamics study of **12o** against AChE. A) RMSD graph of 4EY7 bound to **12o**, **EJMC-4e** and **DPZ**. B) RMSD graph of compound **12o**, **EJMC-4e**, and **DPZ** against 4EY7, C) RMSF plot of 4EY7 bound to **12o**, **EJMC-4e**, and **DPZ**, D) RMSF plot of compound **12o**, **EJMC-4e**, and **DPZ** E) Radius of gyration plot of **12o**, **EJMC-4e** and **DPZ**, against 4EY7.

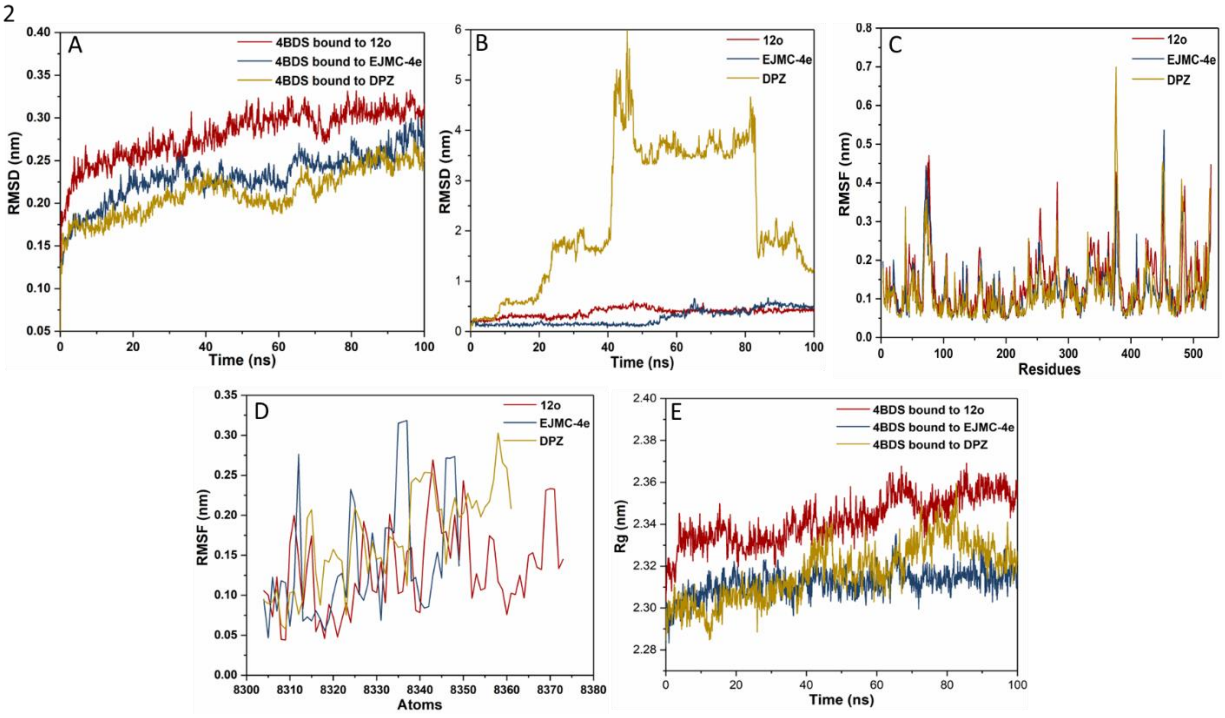

Figure 4.5: Molecular dynamics study of **12o** against BChE. A) RMSD graph of 4BDS bound to **12o**, **EJMC-4e** and **DPZ**. B) RMSD graph of compound **12o**, **EJMC-4e** and **DPZ** against 4BDS, C) RMSF plot of 4BDS bound to **12o**, **EJMC-4e** and **DPZ**, D) RMSF plot of compound **12o**, **EJMC-4e** and **DPZ** against 4EY7, E) Radius of gyration plot of **12o**, **EJMC-4e** and **DPZ**, against 4BDS.

4.3.4 *In-vitro* antioxidant property evaluation of 12o

DPPH (1,1-diphenyl-2-picrylhydrazyl) is a radical compound commonly used to evaluate the antioxidant activity of synthesized compounds *in-vitro*. The assay works by measuring the ability of the compounds to scavenge or reduce the unstable DPPH radical to its stable form. A decrease in the absorbance of the DPPH solution after the addition of the compounds indicates its antioxidant activity, as the compounds react with DPPH and stabilize the free radical. The results are expressed as the IC_{50} value, the compound concentration required to scavenge 50% of the initial DPPH radical. In the DPPH assay, **12o** was found to be the most

prominent activity with IC_{50} = 6.19 ± 0.33 µM compared to compound **EJMC-4e** (IC_{50} = 94.29 ± 0.19 µM). Interestingly, approximately 15 times the antioxidant properties in the lead compound **12o** were significantly enhanced over **EJMC-4e (Figure 4.6)**. As we know, antioxidants play a vital role in scavenging free radicals and ROS. Therefore, we further evaluated its potential against H_2O_2-induced oxidative stress in the PC12 cell line, regulating ROS release potential in human microglial cells' mitochondrial and cellular ROS attenuation properties in the drosophila model. All other tested compounds showed moderate activity in the range of (41 to 55 μM) as shown in **Table 4.2**.

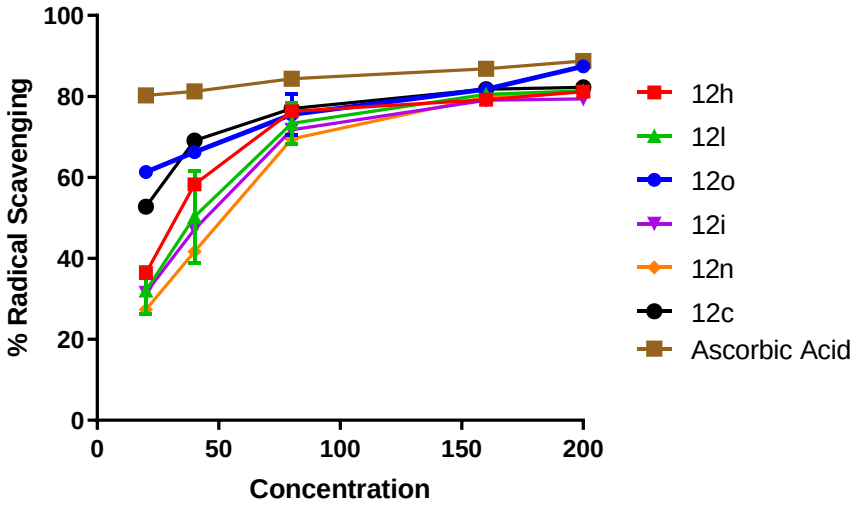

Figure 4.6: Antioxidant study (DPPH assay) of compounds, 12h, 12l, **12o**, 12i, 12n, 12c and ascorbic acid. Results are the means ± SD for the three experiments performed in triplicate.

Table 4.2 DPPH antioxidant assay of compounds 12h, 12i, 12l, 12n, **12o**, **EJMC-4e**, and ascorbic acid.

Code	**% radical scavenging***	IC_{50} (μM)[#]
12h	36.55 ± 0.54	41.42 ± 0.71
12i	31.50 ± 0.62	49.42 ± 0.54
12l	27.00 ± 0.95	54.40 ± 0.83
12n	27.30 ± 0.66	55.49 ± 0.57
12o	61.15 ± 1.16 %	6.19 ± 0.33
EJMC-4e	19.06 ± 0.20	94.29 ± 0.19
Ascorbic acid[1]	80.49±0.23	ND

* % Radical scavenging was calculated at 20 μM Conc. % Radical scavenging;

represents means ± SD of duplicate experiment

[#] IC_{50}**:** Concentration to inhibit 50% activity. Data represent means ± SD of the experiments performed in duplicate

[1]Ascorbic acid = positive control

ND = not determined.

4.3.5 Measurement of propidium iodide displacement from the peripheral anionic site (PAS) of AChE

The study aimed to investigate the effect of compound **12o** on the PAS of AChE, an enzyme involved in regulating neurotransmission. Following our publications, a propidium iodide-based competitive displacement experiment assessed **12o**'s affinity for the PAS of AChEs. A relative change in fluorescence intensity after incubating AChE (5.0 U/ml) with compounds **12o** or FA or **DPZ** (5, 10, 20, and 50 μM) and propidium iodide (**table 4.3)** was measured. It is evident from Table 3 that **12o** effectively displaced propidium iodide by 21.36 ± 0.14, indicating its comparative efficacy to the reference drug **DPZ** (24.38 ± 0.43) at 50μM concentration. The results demonstrated that **12o** can effectively bind to the PAS site of AChE, which presents a potentially valuable therapeutic intervention for regulating neurotransmission.

Table 4.3. The propidium iodide displacement from the PAS of AChE by **12o**, **FA**, and **DPZ** at the described concentration.

Code	**5 μM (%)**	**10 μM (%)**	**20 μM (%)**	**50 μM (%)**
12o	11.32 ± 0.21	15.76 ± 0.31	18.73 ± 0.43	21.36 ± 0.14
FA	0.31 ± 0.12	2.39 ± 0.16	5.38 ± 0.23	8.23 ± 0.17
DPZ	15.38 ± 0.33	17.93 ± 0.25	20.88 ± 0.29	24.38 ± 0.43

[a] Results are reported in mean ± SD for two independent experiments.

4.3.6 *In-vitro* blood-brain barrier permeation assay:

In-vitro blood-brain barrier (BBB) assay is a laboratory method employed to evaluate the capacity of a compound to cross the BBB and gain access to the central nervous system (CNS). We have utilized this tool to evaluate whether our lead compound could penetrate BBB to access CNS. The assay was validated by comparing the experimental permeability values of commercially available drugs such as testosterone (positive control) and norfloxacin (negative control) with their reported values established by Di *et al [168]*. Based on this relationship, compounds with permeability values higher than 4.8×10^{-6} cm s^{-1} could passively diffuse through the blood-brain barrier (**table 4.4**). The results showed that **12o** permeability values exceeded the limit, suggesting it could cross the BBB.

Table 4.4. Permeability (P_e = 10^{-6} cm s^{-1})[a] in the PAMPA-BBB assay for **12o**, **DPZ**, testosterone and norfloxacin with their predictive BBB penetration

S.No.	Compound	P_e (exp)[a]	Literature value	Predictions
1	**12o**	12.07 ± 1.03	------	CNS (+)
2.	Testosterone	18.43 ± 0.39	17.0	CNS (+)
3.	Norfloxacin	0.12 ± 0.04	0.1	CNS (-)
4.	**DPZ**	17.59 ± 1.17	-------	CNS (+)

[a] Represents the average (mean) ± standard deviation (SD) derived from two independent experiments.

[b] Represents literature value referred from Di *et al*.

[c] CNS (+) indicated high permeability with Pe > 4.0, CNS (-) signifies low permeability with Pe < 2.0, and CNS (±) represents uncertain permeability within the range of 2.0 to 4.0.

4.3.7 Evaluation of metal-chelating properties of 12o

It is evident from the literature that the dysregulation of biometals, specifically iron (Fe) and copper (Cu), significantly contributes to AD development. The accumulation of bio-metals in the extracellular environment triggers oxidative stress (OS), resulting in the production of reactive free radical species that are highly toxic. Hence, the modulation of bio-metals for the treatment of AD has been considered an effective therapeutic strategy. The compound **12o**, exhibiting the most prominent enzyme inhibition and antioxidant properties, was selected to assess its metal chelation capacity. The capability of compound **12o** to chelate metal was evaluated through a UV-vis spectroscopy assay (**Figure 4.7**). The experimental procedure involved the combination of equimolar concentrations of **12o** and $FeCl_3.6H_2O$, followed by a comprehensive analysis of the resulting complexation. As shown in **Figure 4.7 A**, the absorption spectra of compound **12o** in the presence of $FeCl_3.6H_2O$ differed from that of compound **12o** in the isolation. The solution's absorption spectra at pH 7.4 displayed a greater magnitude at 511 nm than those observed at lower pH levels (4.2), as depicted in **Figure 4.7A**. This observation provides evidence of a complex formation between **12o** and the Fe (III) ion. The compound **EJMC-4e** was also evaluated against Fe^{3+} for its metal chelation properties (**FFigure 4.7 C**) and found to be devoid of such complexation properties. We also performed metal chelation activity of **12o** against Fe^{3+} and Cu^{2+} using HEPES buffer following the method reported in the literature[159]. We incubated **12o** 1:1 with $FeCl_3$ and $CuSO_4$ and took absorption spectra using a UV spectrophotometer. As shown in (**Figure 4.7 D**), **12o** showed maximum absorption at the wavelength around 240 nm. In the presence of Fe3+ and Cu2+, the

wavelength shifted to 251 and 258 nm, respectively; absorption also dropped. This reveals that **12o** makes a complex with both iron and copper. The interaction between **12o** and Fe^{3+} was studied by gradually adding $FeCl_3.6H_2O$ to **12o** in different molar ratios, and changes in absorption at 511 nm were monitored. Subsequently, the absorbance value was graphed about the mole fraction of **12o**. The isosbestic point (wavelength, wave number, or frequency at which the total absorbance of a sample does not change) shown in **Figure 4.7 B** is at 6.8, indicating a stochiometry of 2.1:1 for the **12o**- Fe^{3+} complex.

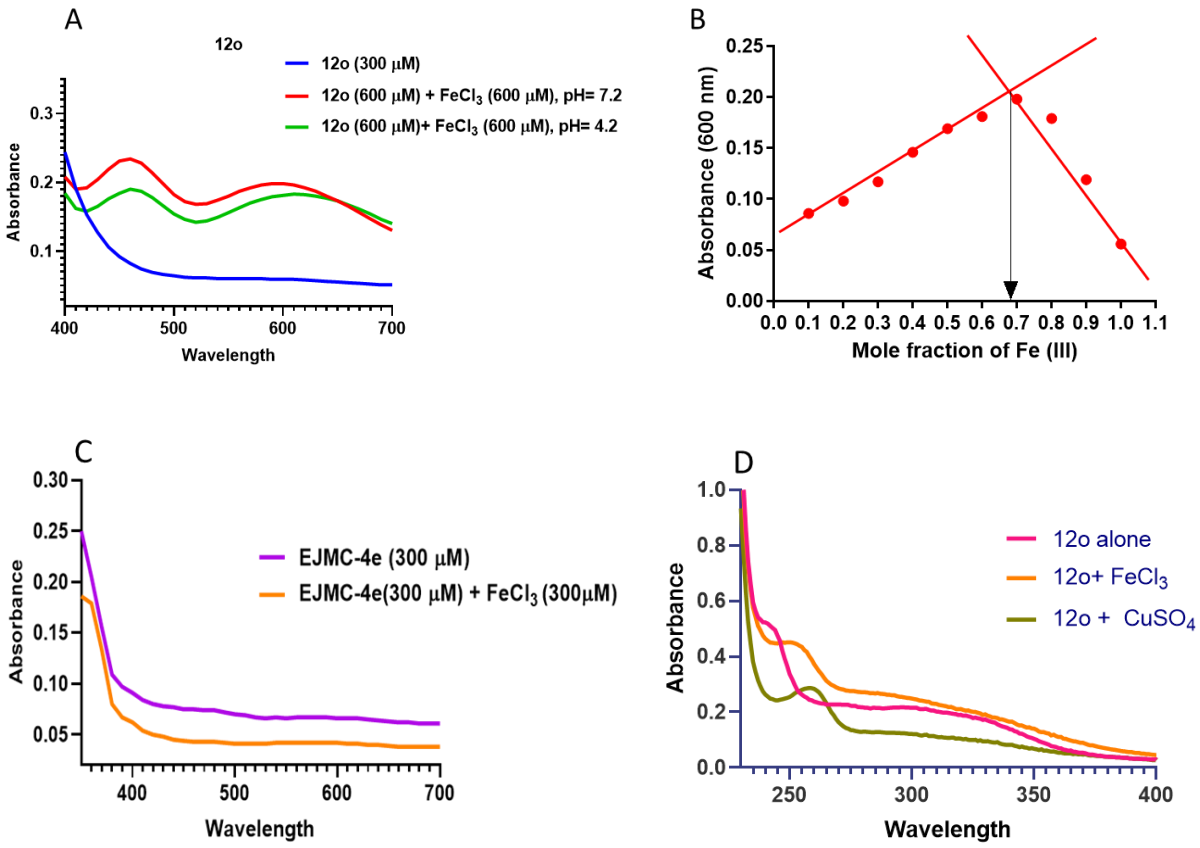

Figure 4.7: Metal-chelating properties of **12o**. (**A**) UV absorbance spectrum of compound **12o** (100 μM) alone or in the presence of $FeCl_3$ (100 μM) in extra pure methanol. (**B**) Job's plot for

compound **12o** against Fe (III). C) Metal chelation activity of **EJMC-4e** against iron. D) Metal chelation of compound **12o** against Fe^{3+} and Cu^{2+} using HEPES buffer.

4.3.8 Modulation of self and metal-induced $A\beta_{1-42}$ aggregation by 12o

ThT assay is a widely used technique for monitoring amyloid aggregation [169, 170]. The findings derived from this assay are significant in elucidating the inhibitory impact of **12o** on $A\beta_{1-42}$ fibril formation. Metal (Cu^{2+} and Fe^{3+}) induced $A\beta_{1-42}$ aggregation through ThT fluorescence assay is widely exploited to quantify the involvement of metals in the fibrillization process. Therefore, metal-induced Aβ aggregation inhibition was performed to evaluate the bivalent inhibitory impact of **12o** via self-induced and metal-induced Aβ aggregation. The data presented in (**Figures. 4.8 A** and **4.8 B**) demonstrated that **12o** has a potent inhibitory effect on the aggregation of $A\beta_{1-42}$. This effect appears to result from the cumulative inhibitory actions of **12o**, which involve its ability to chelate metal ions and its direct interaction with Aβ to prevent the formation of fibrils. We also performed confocal imaging to understand the molecular-level interaction among $A\beta_{1-42}$, FeCl3, and compound **12o**. When $A\beta_{1-42}$ was exposed to the metal, aggressive plaque deposition showed a notable increase (**Figure 4.8.1 B**). In contrast, when we incubated **12o** with Aβ 1-42 and FeCl3 (**Figure 4.8.1 C**), we did not observe the $A\beta_{1-42}$ aggregation plaque, suggesting its potential in reversing or mitigating the effects of the interaction between $A\beta_{1-42}$ and $FeCl_3$. In summary, the results above offer significant perspectives regarding the possible application of **12o** as a preventative intervention for amyloid-associated illnesses, including AD.

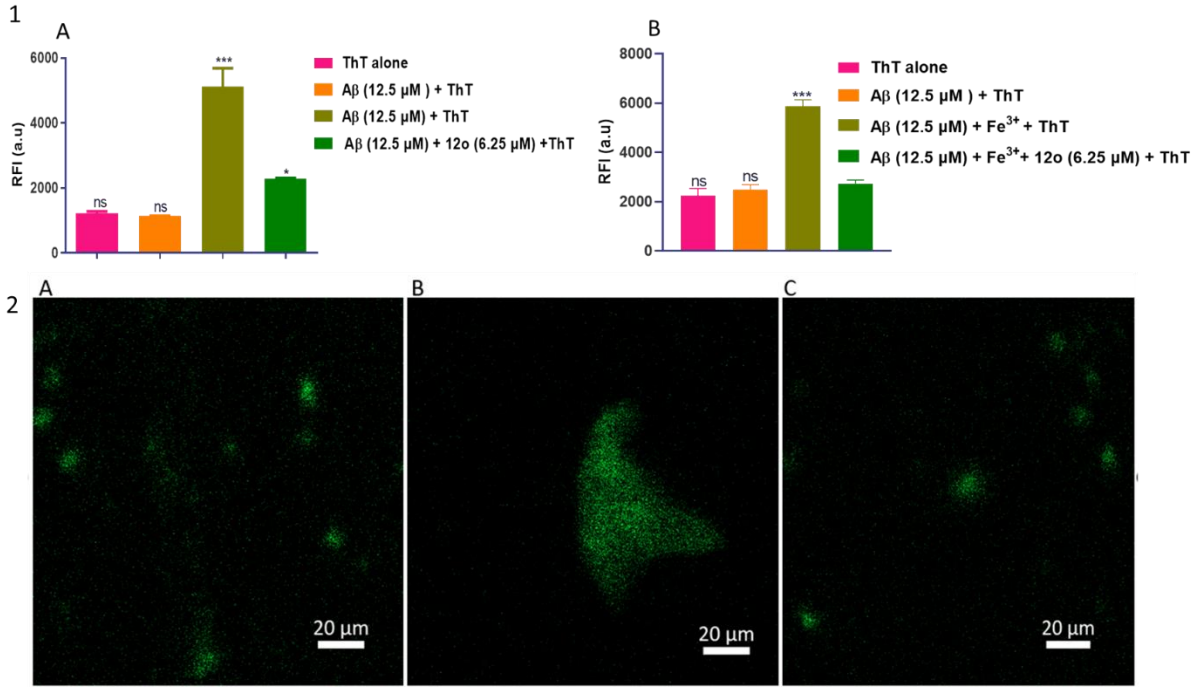

Figure 4.8: The inhibitory effect of compound **12o** on Aβ aggregation. 1. (A) $A\beta_{1-42}$ self-aggregation, and (B) iron-induced $A\beta_{1-42}$ aggregation. Incubation of $A\beta_{1-42}$ alone, or $A\beta_{1-42}$ + **12o** or $A\beta_{1-42}$ + **12o**+iron was carried out for 72 hrs. followed by ThT assay. * indicates $p < 0.05$, and *** denotes $p < 0.001$ and **ns** indicated $p > 0.05$. The data is presented as the mean ± standard error of two independent experiments. 2. Confocal microscopy images were taken to examine three different scenarios: A) ThT and $A\beta_{1-42}$ alone, B) ThT, $A\beta_{1-42}$, and FeCl3, and C) ThT, $A\beta_{1-42}$, FeCl3, and **12o**. These images provide visual insights into the interactions and effects in each experimental condition.

4.3.9 Cell based study on PC12

The cell cytotoxicity and H_2O_2 Induced oxidative stress studies were carried out in **Dr. Saroj Kumar's** laboratory and experiment were performed by **Sanskriti Rai.**

4.3.9.1 Cell cytotoxicity assessment of 12o against PC12

Assessment of cytotoxicity is a crucial aspect of drug development. The *in-vitro* cytotoxicity investigations were conducted before the commencement of the *in-vivo* studies. The molecule **12o**, which exhibited potent inhibitory activity against AChE/BChE and antioxidant and metal chelation properties, was chosen for assessing its cytotoxicity on the PC12 cell line. PC12 cells are commonly employed as an optimal cellular model for evaluating novel therapeutic interventions for AD. Studies have shown that upon differentiation, PC12 cells closely model neurons in terms of morphology and physiological and biochemical functions[171]. Hence, in this study, all the experiments have been performed in differentiated PC12 cells. The PC12 cells were subjected to varying concentrations (1, 2.5, 5, 7,10, 20, and 30 µM) of **12o** for 24 hr (**Figure 4.9**), and the extent of cell mortality was assessed quantitatively using the 3-(4,5-dimethylthiazol-2-yl)-2,5-diphenyltetrazolium bromide (MTT) assay. The experiment showed that **12o** showed no significant cytotoxic effect on PC12 cells at concentrations up to 30 µM.

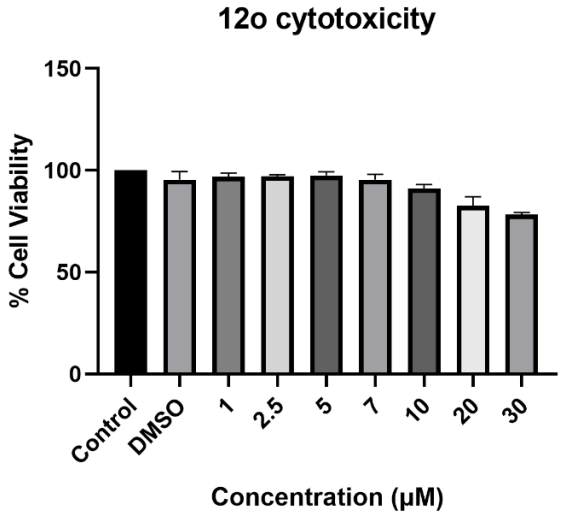

Figure 4.9: The impact of **12o** on cellular viability. The cells were subjected to varying concentrations of **12o** (1, 2.5, 5, 7, 10, 20 and 30 μM) for 24 hr. The MTT assay was utilized

to analyze cell viability, expressed as a percentage. All assays were performed using samples in quadruplicate and presented as mean ± SE.

4.3.9.2 Assessment of neuroprotective activity against H_2O_2-induced oxidative stress

12o was found to be a promising lead able to quench free radicals generated under DPPH assay, which strongly suggested that **12o** is a potent antioxidant with a potency approximately 15 times (IC_{50} = 6.19 ± 0.33 µM) compared to the parent natural compound **EJMC-4e (**IC_{50} = 94.29 ± 0.19 µM). Studies have also reported oxidative stress as a prominent contributor to AD pathology, principally by promoting neurodegeneration through an array of molecular mechanisms that disrupt neuronal homeostasis. [2]. In this study, we assessed the protective effect of **12o** against oxidative stress induced by H_2O_2, which is commonly used to trigger cellular oxidative stress. [172]. The PC12 in the concentration of $1x10^4$ cells/well were seeded in a 96-well plate and incubated with **12o** for 24 hr at 20 µM, 10 µM, 7 µM, 5 µM, 2.5 µM, and 1 µM concentrations; the following cells were treated with 600 µM of H_2O_2 to induce oxidative stress (concentration of H_2O_2 producing ~ 50% cell death, **Figure 4.10 A & B**). The H_2O_2-treated group, in the absence of **12o**, exhibited 46.32% cellular viability. However, when incubated with **12o** compound at a concentration of 20 µM, cellular viability significantly increased to 79.56%. These findings suggest that **12o** effectively mitigates H_2O_2-induced oxidative stress, highlighting its antioxidative properties, thus making it a potential candidate in AD therapeutics.

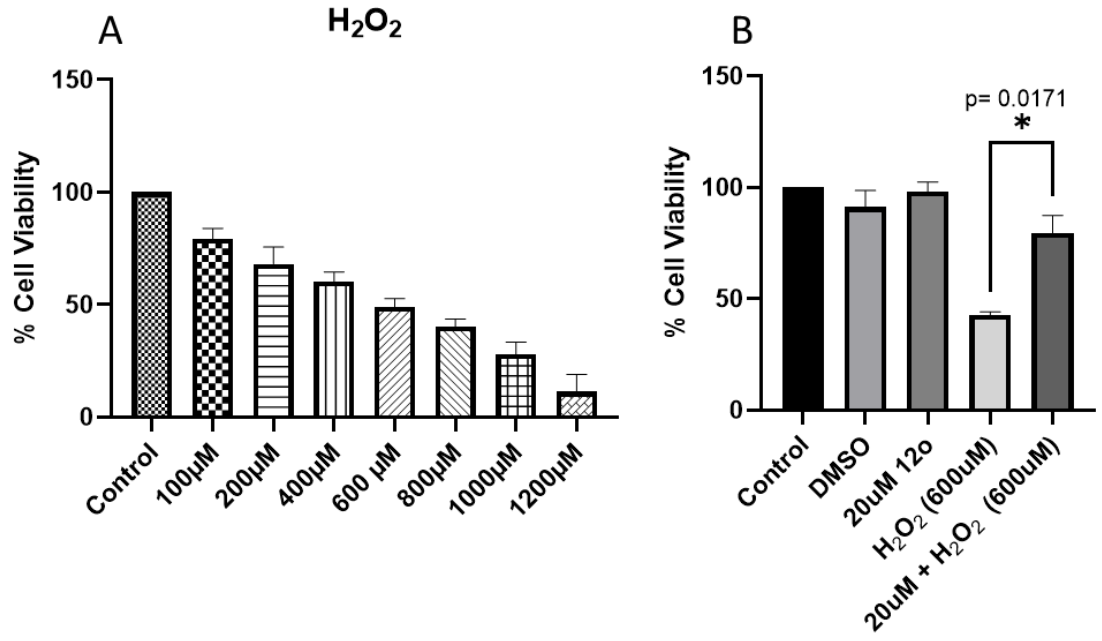

Figure 4.10: Neuroprotective assessment of compound **12o** against H_2O_2 induced oxidative stress. A) Cell viability assay at different concentrations (100, 200,400, 600, 800,100, 1200 µM) of H_2O_2. B) Effect of **12o** on the cell viability in H_2O_2 (Test applied: Unpaired t-test with Welch's correction). Data represents the mean ± SD of at least three independent experiments.

4.3.10 Evaluation of lead compounds against NLRP3 inflammasome

The NLRP3-related experiments were carried out in **Dr. VGM Naidu's** laboratory, and these experiments were performed by **Samir Kumar Panda**.

4.3.10.1 Evaluation of 12o against ROS release and its effect to mitochondrial membrane potential.

The two processes that appear to be responsible for the NLRP3 inflammasome cascade are the priming and activation stages. Toll-like receptor 4 (TLR4) agonists, such as LPS, start the priming procedure through the TLR/NF-κB signaling pathway by encouraging the creation of precursor proteins such as NLRP3, pro-IL-18, and pro-IL-1β. The NLRP3 inflammasome

complex assembles during activation, prompted by stimuli like ATP. The cysteine protease pro-caspase-1 is recruited during the activation step under the direction of ASC, and it collaborates with CARD to facilitate the formation of the NLRP3 inflammasome. Pro-IL-1β and pro-IL-18 mature into active forms after pro-caspase-1 cleaves to become active caspase-1. The *in-vitro* experimental timeline is shown in **Figure 4.11A**. **12o** compound was treated at varying doses in HMC-3; a dose of 12.5µM and 25µM enhanced the microglial cell proliferation. Following the cell viability experiment, LPS+ATP primed microglial cells were treated with varying doses of compound **12o**, and a dose of 12.5µM was found to inhibit the LPS+ATP-induced cytotoxicity. Therefore, the successive experiments involved using a **12o** compound at a dose of 12.5µM (**Figure 4.11B**).

Our work evaluated the estimation of mitochondrial ROS and its membrane potential disrupted by inducing agents such as LPS+ATP and further explored the effect of **12o** in attenuating the mitochondrial ROS and restoring the mitochondrial membrane potential, as shown in **Figure 11**. Inhibiting ROS production and restoring the MMP is crucial in treating AD. Compound **12o** significantly inhibited ROS generation (**Figure 4.11C, D**) in DHE staining compared to the LPS+ATP primed group. Similarly, LPS+ATP treatment disrupted the MMP of the microglial cells, and treatment with compound **12o** regulated the MMP compared to the CP group (**Figure 4.11E, F**). These results confirm the potential effect of combination **12o** in regulating the ROS levels and MMP of the mitochondria in microglial cells.

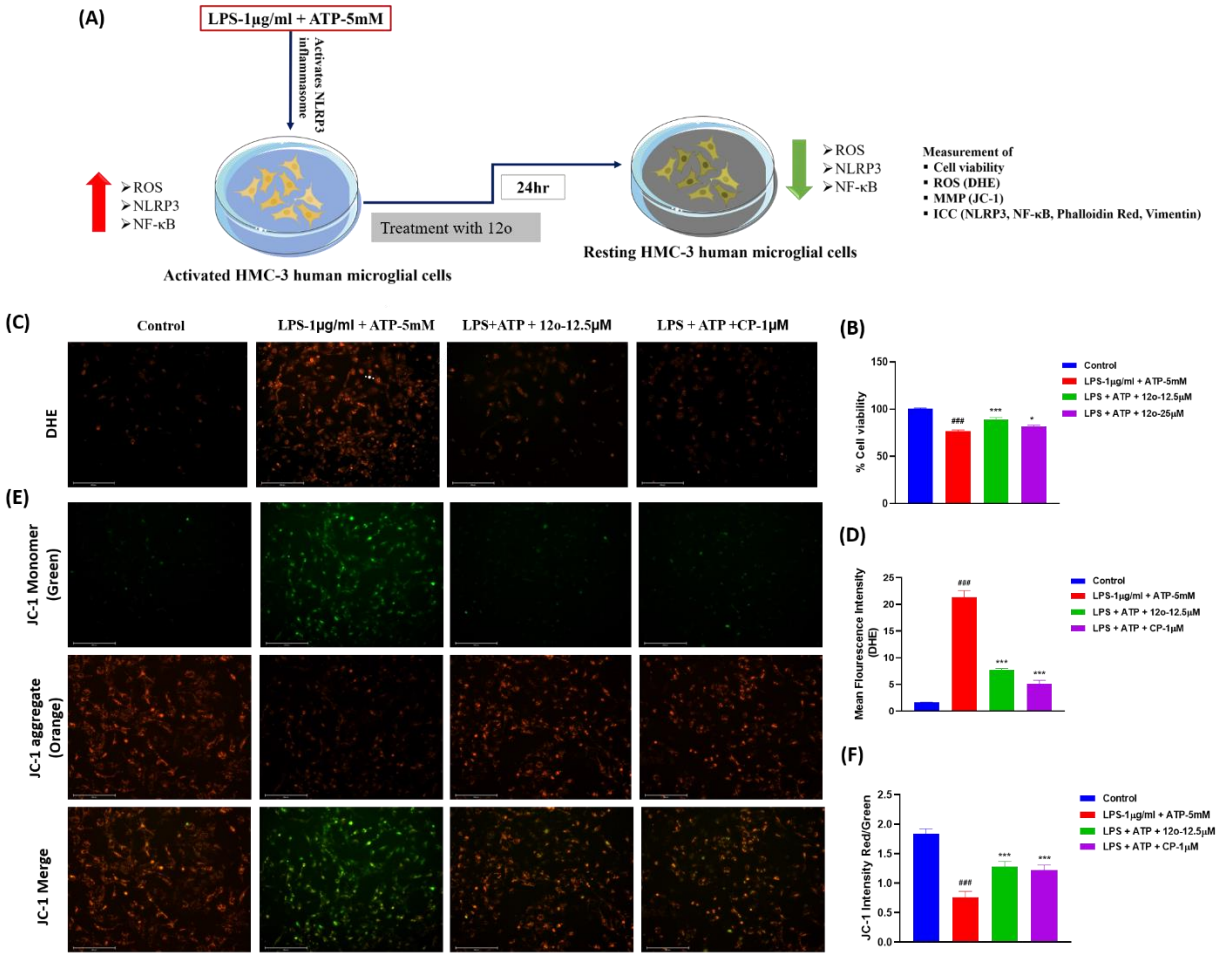

Figure 4.11: **12o** exerted microglial cell proliferation and attenuates the ROS and MMP damage caused by LPS and ATP. A) Graphical representation depicting the *in-vitro* experimental design. B) To check the proliferative effect of compounds against NLRP3 inflammasome-mediated inflammation, HMC-3 cells were primed with LPS (1 µg/ml) and ATP (5 mM). Further, cells were treated with the test compounds at 12.5 µM. Compound **12o** showed a significant increase in microglial proliferation compared to the LPS+ATP-treated group. C) Representative images of DHE staining in HMC-3 cells and D) Bar Graph of DHE assay. E, F) JC-1 stained HMC-3 cells and Bar graph to study the MMP. All the data were analyzed as mean ± SD (n=3). Statistical significance was further determined by one-way

ANOVA followed by Tukey's test in which the LPS+ATP group was compared with a standard control, where statistical significance was defined as #p<0.05, ##p<0.01, and ###p<0.001, and *p<0.05, **p<0.01, and ***p<0.001 represent LPS+ATP vs **12o** respectively.

4.3.10.2 Evaluate 12o against NLRP3 inflammasome and NF-κB expression.

Recent research has shown NLRP3 inflammasome inhibitors' crucial role in treating neuroinflammation and neurodegenerative diseases such as AD. Tau aggregates have also been linked to NLRP3 activation in mice, a mouse model that overexpresses the human tau protein with the P301S mutation. The link between NLRP3 inflammasome activation and tau pathology exacerbates and drives tau pathology in AD mouse models. Thus, inhibiting inflammasome activation serves as a potential strategy for treating AD. Targeting nuclear factor-kappa B (NF-κB) and NLRP3 inflammasome activation by P2X7/NLRP3/caspase one pathway may be a sensible strategy to combat AD pathogenesis as neuroinflammation and neurodegeneration are closely connected and play a vital role in the disease progression. The expression of NF-κB (**Figure 4.12 A, B**) and NLRP3 (**Figure 4.12 C, D**) was significantly reduced after treatment with compound **12o** when compared to LPS+ATP primed cells, pointing to the compounds' anti-inflammatory and anti-microglial activity. The chemical moieties also successfully reduced microglial activation and increased vimentin levels (**Figure. 4.12C, E**). Vimentin deletion causes altered microglial function and morphology, according to previous investigations [72]. These results demonstrate the potential effect of the synthesized compound **12o** in attenuating neuroinflammation and neurodegeneration.

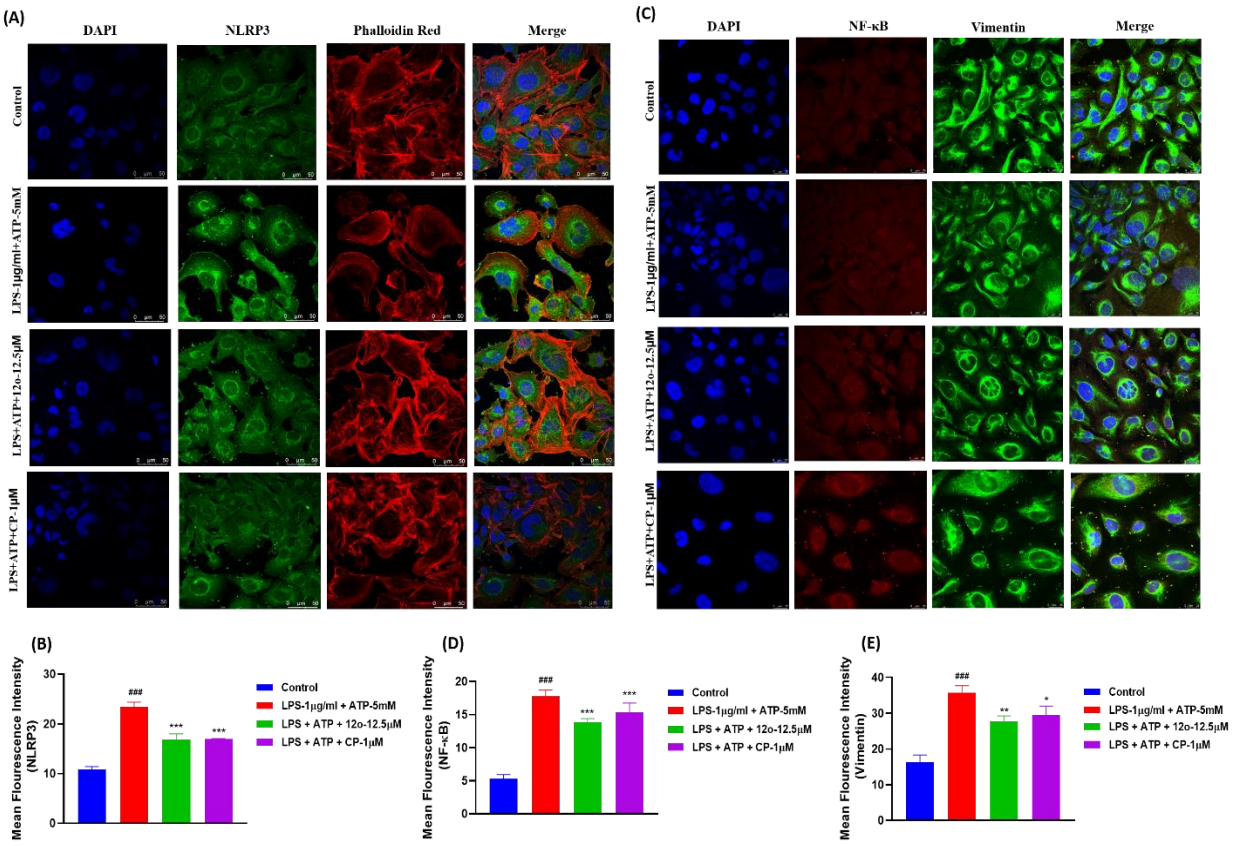

Figure 4.12: Compound **12o** inhibited microglial activation and reduced the NF-κB and NLRP3 inflammasome activation as evidenced by Immunocytochemistry (ICC) staining of HMC-3 cells for NLRP3, NF-κB, Vimentin, and Phalloidin Red. A, B) HMC-3 cells stained with DAPI (nuclear stain), NLRP3 (Green), and Phalloidin red (Red) to assess NLRP3 inflammasome expression and microglial activation and Bar graph representing the Mean Fluorescence intensity of NLRP3. C, D, and E) Confocal images and bar graph illustrating the HMC-3 cells stained with NF-κB and Vimentin. All the data were analyzed as mean ± SD (n=3). Statistical significance was further determined by one-way ANOVA followed by Tukey's test in which the LPS+ATP group was compared with standard control, where statistical significance was defined as #p<0.05, ##p<0.01, and ###p<0.001, and *p<0.05, **p<0.01, and ***p<0.001 represent LPS+ATP vs. **12o** respectively.

The NLRP3 inflammasome causes caspase-1 activation and the release of proinflammatory cytokines in activated microglia. Immunoblotting of NLRP3 and Caspase-1 confirms the role of LPS and ATP in activating dual signals and further aggravating inflammation. Inhibiting the NLRP3 activation and caspase-1 is a potential strategy for halting microglia activation-mediated neuroinflammation and neuronal death (**Figure 4.13 A**). Compounds at a dose of 12.5 and 25µM significantly inhibit the increased NLRP3 activation (**Figure** 4.13 C) by LPS and ATP and further show a marked decrease in caspase-1 levels (**Figure 4.13 B**). These results confirm the dose-dependent effects of compound **12o** in attenuating the NLRP3 inflammasome signaling cascade.

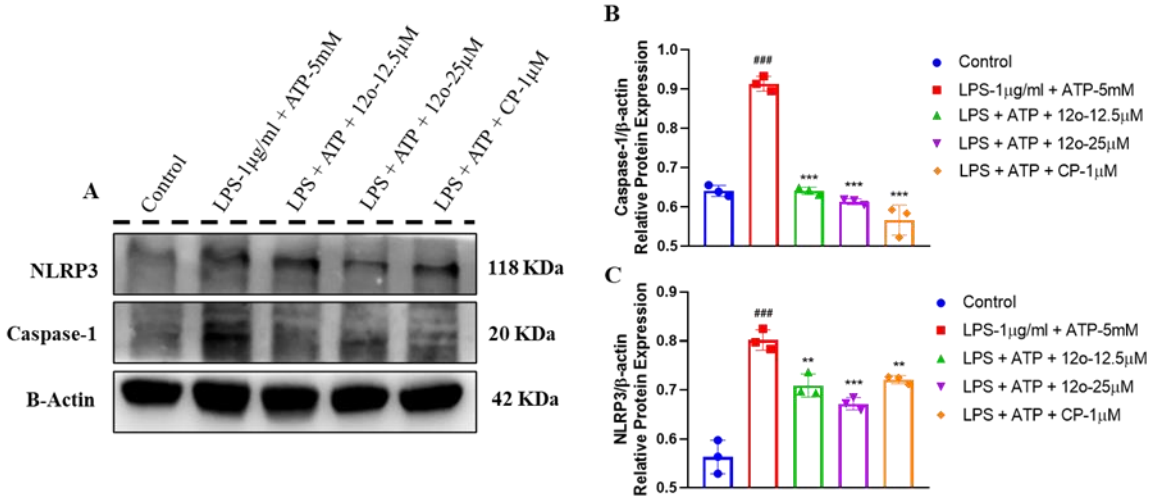

Figure 4.13: Compound **12o** treatment to HMC-3 cells inhibits the NLRP3 inflammasome activation and caspase-1 release. (A) Immunoblotting images of NLRP3, Caspase-1, and B-Actin. (B) Graphical representation of Caspase-1 relative protein expression in HMC-3 cells. (C) Graphical representation of NLRP3 relative protein expression in HMC-3 cells activated with LPS+ATP. All the data were analyzed as mean±SD (n=3). Statistical significance was further determined by one-way ANOVA followed by Tukey's test in which the LPS+ATP

group was compared with the control, where statistical significance was defined as #p<0.05, ##p<0.01, and ###p<0.001, and *p<0.05, **p<0.01, and ***p<0.001 represent LPS+ATP vs **12o** respectively.

4.3.11 Evaluation of 12o in transgenic Drosophila model of AD.

The experiments related to Drosophila were conducted in **Dr. S. Srikrishna's** laboratory. Prabhat Kumar performed these experiments, and I contributed partially to these experiments.

4.3.11.1 Therapeutic effects of 12o and DPZ on OregonR+ an AD model of Drosophila

The different concentrations of **12o** and **DPZ** drugs were administered to OregonR+ to determine the median lethal dose (LD_{50}). The OregonR+ flies grown in normal food did not show lethality, exhibiting 100% eclosed flies. While flies grown in **12o** at 0.05 mg/ml showed 91.98% eclosed flies, 0.1 and 0.2 mg/ml exhibited approximately 90% eclosed flies, whereas the 1 mg/ml exhibited only 60% eclosed flies [**Figure**. 4.14(A)]. Thus, **12o** at 0.05, 0.1, and 0.2 mg/ml did not show any toxicity for fly development and can be recommended for future application against AD. Similarly, the standard drug **DPZ** showed 78% eclosed flies at 100 μM/ml concentration. At the same time, it exhibited approximately 68%, 51%. and 45% eclosed flies at 200 μM/ml, 400 μM/ml, and 800 μM/ml, respectively [(**Figure** 4.14 B). Thus, **DPZ** showed less toxicity at 100 μM/ml concentration, so this concentration of **DPZ** was considered for further studies.

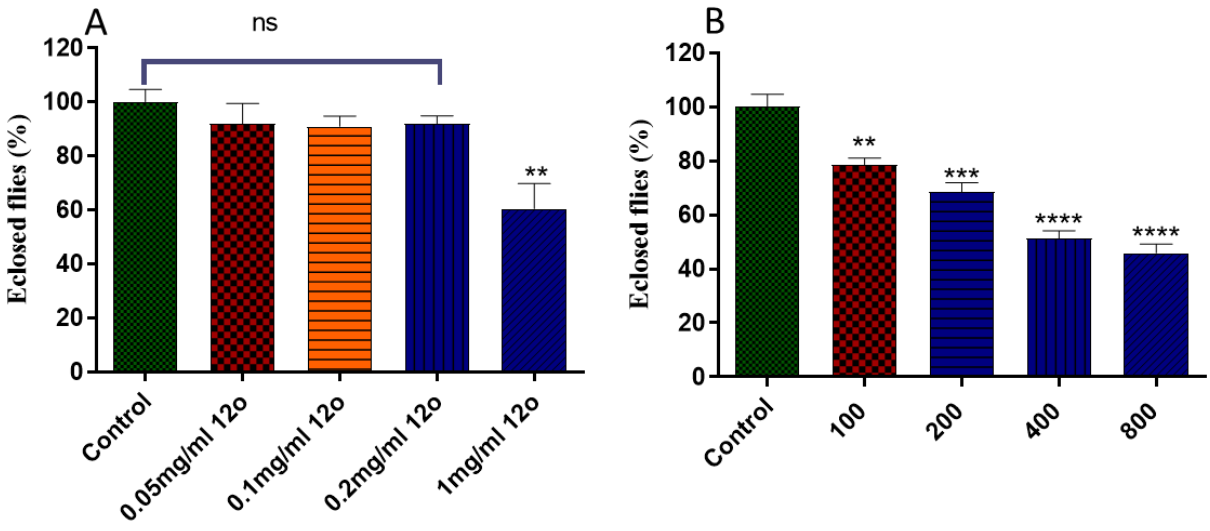

Figure 4.14: The toxicity studies of compound **12o** and **DPZ** in the Drosophila model. A) Toxicity studies of compound **12o** at different concentrations (0.05, 0.1, 0.2, and 1 mg/ml). B) Toxicity studies of standard donepezil at different concentrations (100, 200, 400, and 800 µM). Statistical analysis was performed using one-way ANOVA followed by the Dunnet test, where "*ns*" represents not significant, **p<0.01, *** p<0.001, **** p<0.0001 compared to the control group.

4.3.11.2 Effect of 12o on mitochondrial and total cellular ROS and oxidative stress in the Drosophila model of AD.

The study measured mitochondrial superoxide levels using MitoSOXTM Red as an indicator. In untreated 3rd instar larval eye imaginal discs of the AD model, there was a 4.5-fold increase in superoxide compared to the control [(**Figure**. 4.15, i (a, b)], and [**Figure**. 14, ii (a., b.)]. However, when AD larvae were treated with **12o** at 0.05mg (127.18 µM)/ml, the superoxide levels were similar to the control **[Figure 4.15, i (a, c), and Figure 4.15 ii (a., c.)**] and reduced

to 1.123-fold. At higher concentrations of 0.1 mg (254.36 µM)/ml and 0.2 mg (508 µM)/ml, **12o** showed 1.37-fold [**Figure 4.15 i & ii (a, d and a., d.)**], and 1.75-fold [**Figure 4.15 I & ii (a, e and a., e.)**] of superoxide levels, respectively, in the AD larval eye imaginal discs. In contrast, the standard drug **DPZ** treatment resulted in 2-fold superoxide levels compared to the control [**Figure 4.15 I & ii (a, d and a., d.)**]. These findings indicated that **12o** is more effective at lower doses (0.05 mg/ml) than higher doses (0.1 mg/ml and 0.2 mg/ml) in attenuating excess mitochondrial superoxide in the AD Drosophila model.

The study also examined the total cellular ROS levels using H2DCFDA in OregonR+ and AD larval eye imaginal discs treated with **12o** and **DPZ**, compared with untreated AD larval eye imaginal discs. The AD larval eye imaginal discs exhibited a 4.85-fold higher level of cellular ROS than the control [**Figure 4.16, i (a, b), and Figure 4.16, ii (a, b)**]. When AD larvae were treated with **12o** at 0.05 mg (127.18 µM)/ml, 0.1 mg (254.36) µM/ml, and 0.2 mg (508.73) µM/ml, it could significantly reduce excessive cellular ROS from 4.85-fold to 1.28, 1.57, and 2-fold, respectively, compared to the control [**Figure 4.16, I (a, c, d, e), and Fig. 15 ii (a., c., d., e.)]**. However, the standard drug **DPZ**, at a concentration of 100 µM, reduced cellular ROS levels equal to the control group [**Figure 4.16, i (a, f), and Figure 15, ii (a., f.)].** These results strongly suggest that **12o**, particularly at the lower concentration of 0.05 mg/ml, can be more effective in protecting against oxidative stress in the AD Drosophila model.

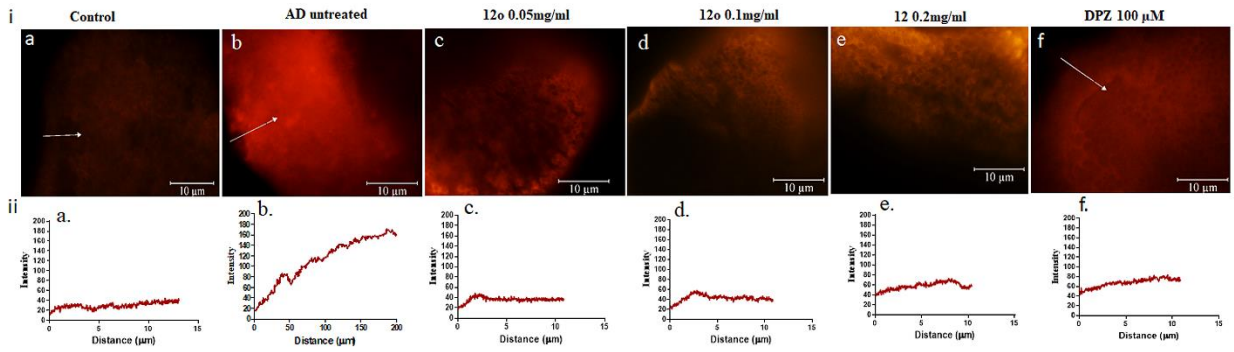

Figure 4.15: Mitochondrial superoxide (ROS) level measurement in Oregon+ and Aβ42 expressing eye imaginal discs of Drosophila. Fluorescence images of 3rd instar larval eye imaginal discs showing MitoSOX Red staining. i. **a**. Control, **b**. AD untreated, **c**. AD treated with **12o** 0.05 mg/ml, **d**. AD treated with **12o** 0.1 mg/ml, e) with **12o** 0.2 mg/ml, f) **DPZ** 100 μM ii. Line graph showing the MitoSOX Red fluorescence intensity in each group's 3rd instar larval eye imaginal discs. The line graphs depicted intensity on the Y-axis and distance (µm) on the X-axis.

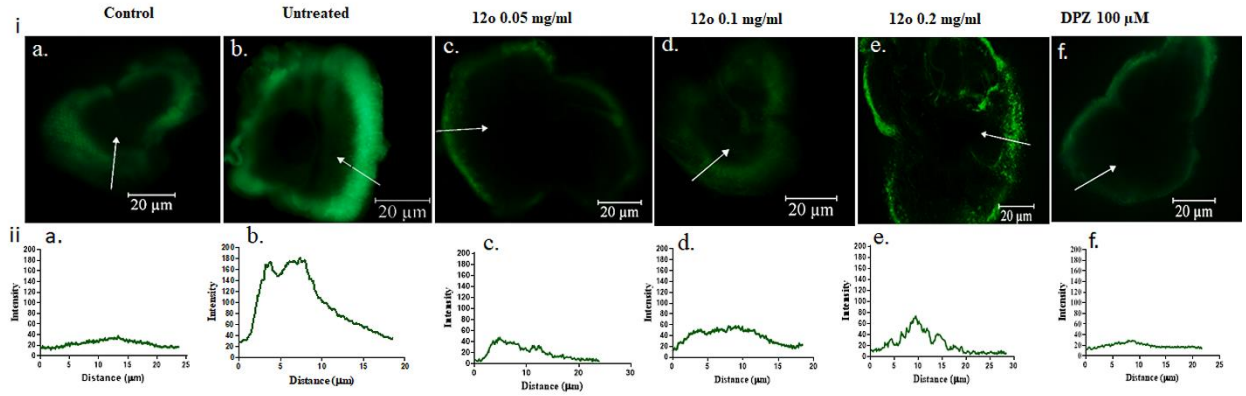

Figure 4.16: Measurement of total cellular ROS level in OregonR+ and Aβ42 expressing eye imaginal discs of Drosophila. Fluorescence images of 3rd instar larval eye imaginal discs showing H2DCFDA staining. i. a) Control, b) AD untreated, c) AD treated with **12o** 0.05

mg/ml, d) AD treated with **12o** 0.1 mg/ml, e) AD treated with **12o** 0.2 mg/ml, f) **DPZ** 100 µM. ii. Line graph showing the H2DCFDA fluorescence intensity in each group's 3rd instar larval eye imaginal discs. The line graphs depicted intensity on the Y-axis and distance (µm) X-axis in situ ROS produced in eye imaginal discs of the control, untreated group, **12o** treated, and **DPZ** treated AD model of Drosophila drawn by NIS-Elements BR 4.3 software.

4.3.12 *In-vivo* evaluation of 12o

I conducted animal experiments in the Department of Pharmaceutical Engineering and Technology IIT (BHU) under Dr. Prashanta Kumar Nayak's supervision, with Himanshu Verma's assistance.

4.3.12.1 *In-vivo* acute toxicity and hepatotoxicity studies with 12o

The acute toxicity and hepatotoxicity were performed on healthy male Swiss albino mice (25-30g), following the OECD (420) guidelines and our previous publication for determining acute toxicity[173]. The mice were administered **12o** (550 mg/kg) and kept under observation for 14 days for any symptoms of toxicity such as death, changes in water or food consumption, abnormal behavior, rashes on skin, or weight loss. However, no such symptoms were observed. On the 14th day, all mice were humanly euthanized and sacrificed, and their livers were microscopically examined for any signs of damage, but none were found. These results indicate compound **12o** did not exhibit acute toxicity or cause liver damage in the mice at the tested dose (**Figure** 4.17 A&B).

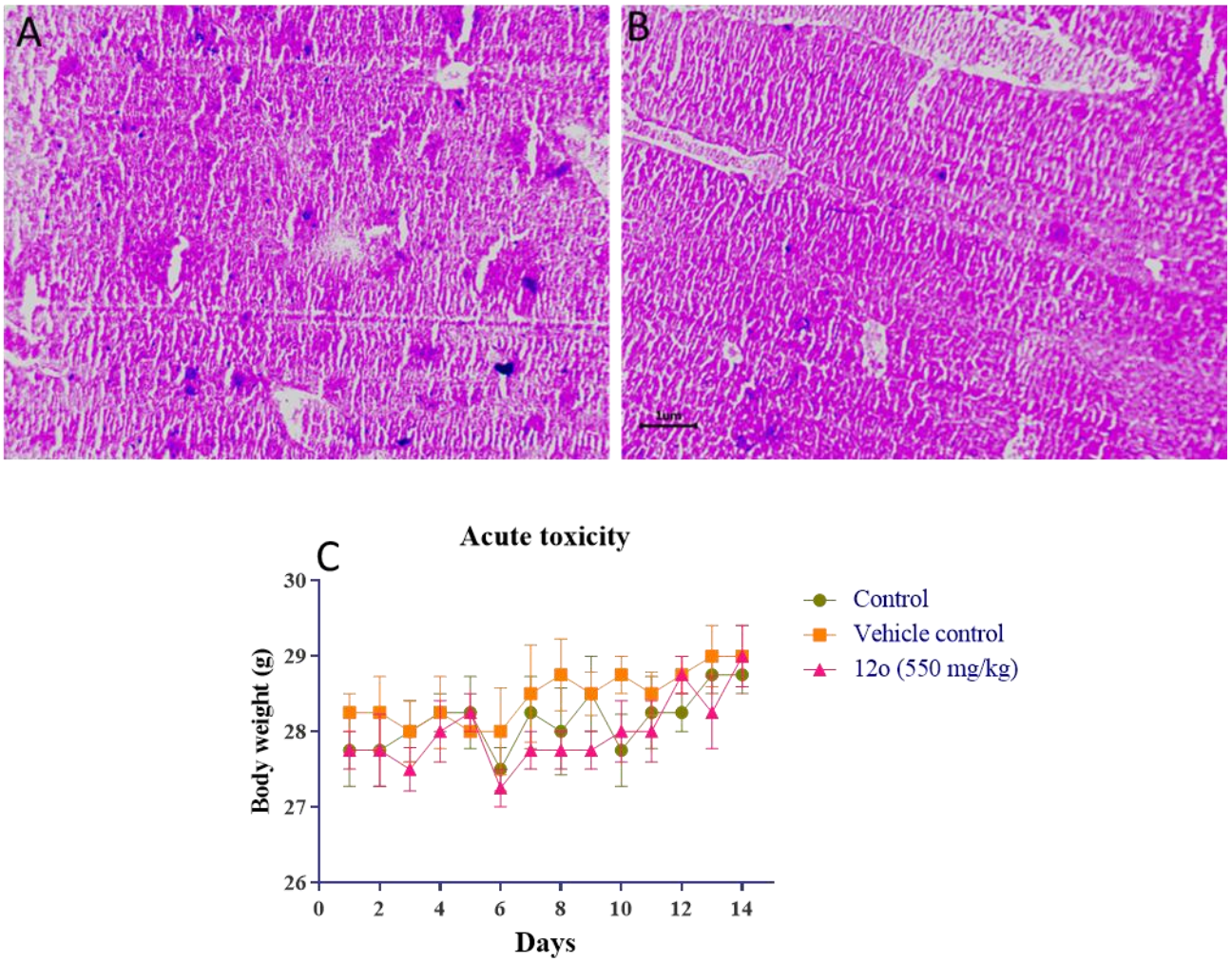

Figure 4.17: Histopathological view of mice liver. A) Vehicle control (no treatment) B) treated group **12o** 550 mg/kg. C) The body weight of control, vehicle control, and compound **12o** (550 mg/kg) treated group. All values are represented as mean ± SD, N = 6 mice per group. Statistical analysis was performed using two-way ANOVA followed by Bonferroni test $P > 0.05$.

4.3.12.2 Assessment of in vivo efficacy of 12o in scopolamine-induced cognitive deficit in the Morris Water Maze test.

The scopolamine-induced amnesia model assessed the *in-vivo* anticholinesterase (anti-ChE) activity of the most efficacious compound **12o** within the series. The use of scopolamine-induced amnesia in rodents is a widely recognized and established model in the field of behavioral pharmacology [148, 174]. This model is commonly employed to assess the inhibitory potential of drug candidates against cholinesterase (ChE), an enzyme involved in memory and learning. The administration of scopolamine results in the selective inhibition of muscarinic cholinergic receptors, thereby causing a notable decline in cognitive functioning. The Morris water maze (MWM) test was employed to assess the anti-amnesic properties of **12o**. Throughout the final five days of the treatment period (day 18 to day 22), body weight and the escape latency time (ELT) of animals of all the experimental groups were recorded (**Figure**. **4.18 A** & **B**). The administration of scopolamine (1.4 mg/kg, i.p.) resulted in a significant increase in escape latency time. The administration of donepezil at 1 mg/kg (i.p.) resulted in a substantial decrease in escape latency time compared to the scopolamine-treated group. Compound **12o** (1 mg/kg, i.p.) did not significantly change escape latency time at an equivalent dose corresponding to **DPZ**. By contrast, at the dose of 5 mg/kg (i.p.), **12o** significantly shortened escape latency time compared to the scopolamine-treated group (**Figure 4.18 B**). The results revealed that **12o** reverses the effect of scopolamine-induced amnesia and improves cognitive impairment against the scopolamine-induced AD-like phenotype. The body weights of the animals remained indifferent among groups, ruling out any impact of differences in body weight on the performance of animals in the Morris water maze (**Figure** 4.18 A).

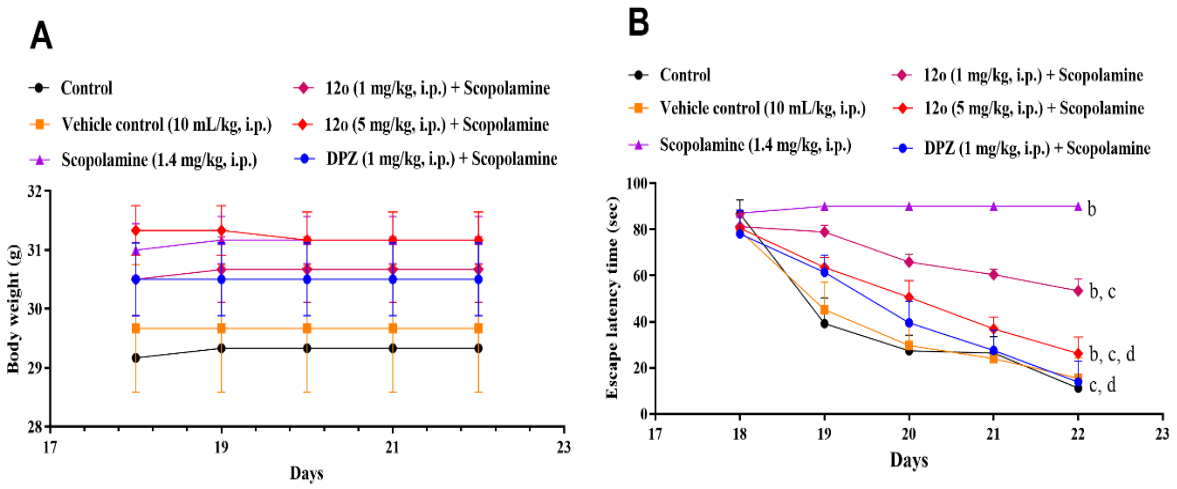

Figure 4.18: The study utilized a scopolamine-induced cognitive impairment mouse model. (A) The daily body weight profile of each group was recorded and analyzed. (B) The escape latency time (in seconds) during the last five days (from day 18 to 22) was recorded and compared among the different groups. All values are represented as mean ± SD, N = 6 rats per group. $^{a}P < 0.05$ versus Control, $^{b}P < 0.05$ versus the vehicle control group, $^{c}P < 0.05$ versus the scopolamine group, $^{d}P < 0.05$ versus **12o** (1 mg/kg) group, $^{e}P < 0.05$ versus **12o** (5 mg/kg) group. Data were analyzed using two-way ANOVA followed by the Bonferroni test.

4.3.13 *Ex-vivo* estimation of AChE and BChE

In subsequent investigations, we assessed the impact of compound **12o** on the levels of AChE and BChE in the brains of mice (**Figure 4.19 A & B**). This was accomplished by employing Ellman's method, which was previously detailed in our report. The administration of scopolamine resulted in a notable increase in the levels of AChE and BChE compared to the control group that received a vehicle treatment. Nevertheless, the increased concentrations of AChE and BChE were notably reduced upon administration of **12o** at a dosage of 5 mg/kg. The lead compound exhibited comparable efficacy to **DPZ** (1 mg/kg), although at higher

dosages than DPZ. The findings indicate that **12o** effectively reduces the elevated levels of AChE and BChE, demonstrating its pharmacological impact on the cholinesterase enzyme.

4.3.13.1 Estimation of neurochemical parameters

To better understand the underlying mechanism behind the anti-amnesic effect of **12o**, we analyzed malondialdehyde (MDA) levels in the brain. This analysis was performed after the Morris Water Maze (MWM) test, utilizing a methodology previously described in our published work [147]. The administration of scopolamine resulted in a significant increase in malondialdehyde (MDA) compared to the control and vehicle-treated groups. However, administration of **12o** resulted in a notable reduction in the MDA level (**Figure 4.19 C**). Thus, the findings demonstrated that compound **12o** possesses better *in-vivo* antioxidant properties than **DPZ**. These results support that it is worthwhile to do further tests to see if **12o** could be useful for treating AD.

The levels of superoxide dismutase (SOD), an antioxidant enzyme that plays a crucial role in protecting the brain against oxidative stress, exhibited a notable decrease when treated with scopolamine compared to the control and vehicle-treated group. In contrast, the study demonstrated the ability of the lead compound **12o** to effectively restore the diminished levels of SOD in animals treated with scopolamine (**Figure 4.19 D**). This implies that these molecules might exhibit neuroprotective properties and potentially mitigate the cognitive deficits induced by scopolamine. The treatment with the lead molecule **12o** may be an effective way to increase the levels of SOD in the brains of mice that have been treated with scopolamine, potentially protecting against the adverse effects of scopolamine on memory and cognitive function.

The antioxidant defense system called catalase (CAT) decomposes hydrogen peroxide into water and oxygen. Hydrogen peroxide is classified as a ROS that can potentially induce oxidative stress, a condition associated with various diseases and the aging process. CAT helps to reduce ROS levels and protect cells from damage. The study described that scopolamine treatment reduces the levels of CAT in the brains of treated animals compared to vehicle and control groups. The reduction in CAT levels suggests that scopolamine may increase oxidative stress in the brains of treated animals. On the other hand, treatment with compound **12o** was found to significantly elevate the levels of CAT in the brains of the treated animals (**Figure 4.19 E**). This observation indicates that compound **12o** exhibits promising antioxidant properties, which may contribute to mitigating oxidative stress and cellular protection against damage. The findings presented in this study offer empirical support for the antioxidant capacity of compound **12o**.

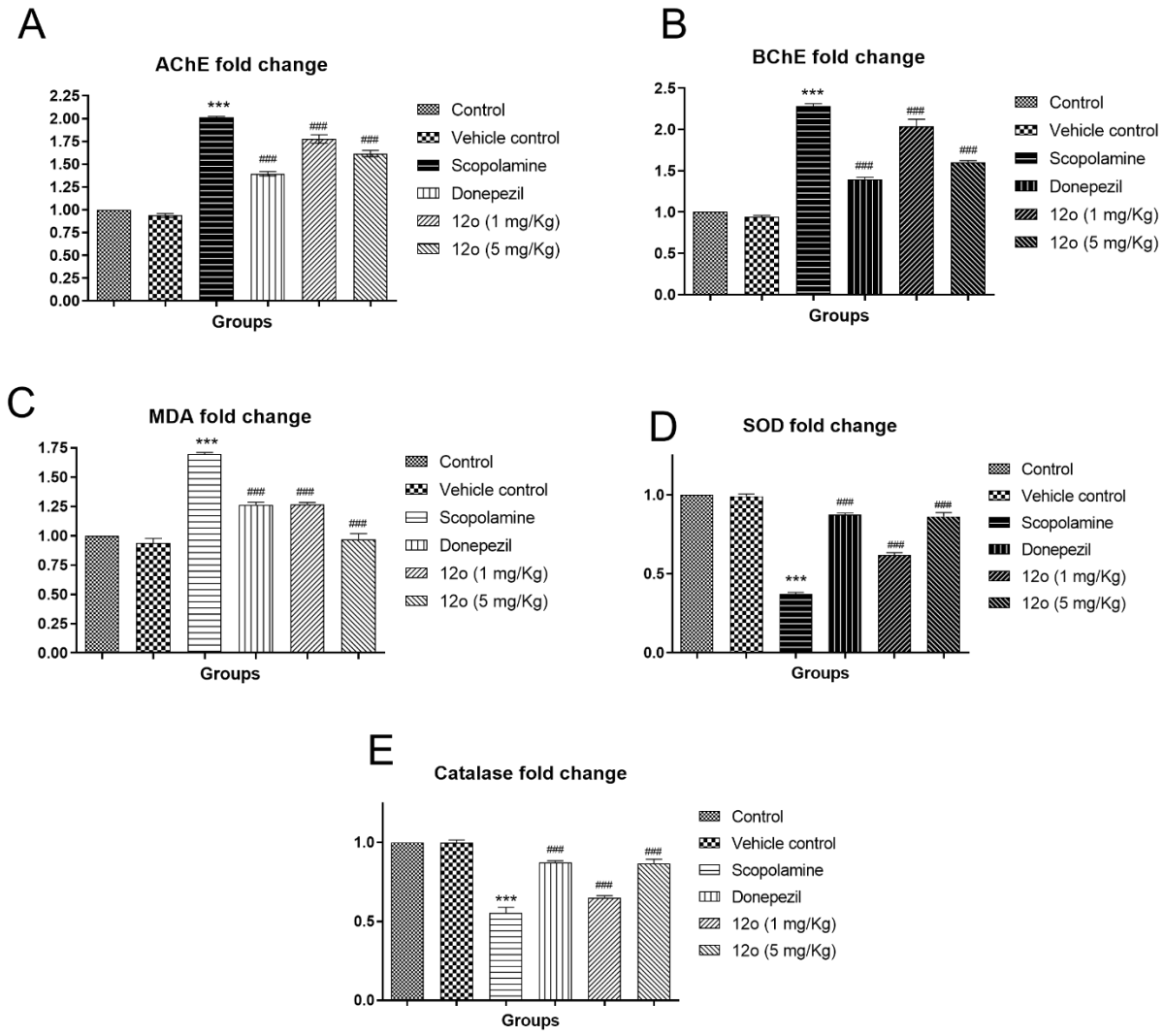

Figure 4.19: Effect of **12o**, **DPZ**, and scopolamine on various neurochemical parameters such as AChE, BChE, MDA, SOD, and CAT levels. A) **12o** regulates elevated AChE levels, suggesting cholinergic function regulation. B) **12o** significantly reduces BChE levels induced by scopolamine, inhibiting BChE activity. C) **12o** enhances SOD activity, displaying antioxidant effects. D) **12o** reduces MDA levels, mitigating oxidative damage. E) **12o** influences CAT activity, countering oxidative stress. Data are expressed as mean ± SEM (n =

6), ***p < 0.001 vs. vehicle control; ###p < 0.001 vs. scopolamine group (One-way ANOVA followed by Tukey's multiple comparison test).

4.4 Rationale behind the design of the Second series of FA hybrid analogs

Complex pathogenic events in AD are intricately interconnected, so targeting a single factor may not constitute a definitive cure. Therefore, the last few decades have witnessed the development of novel scaffolds in the field of AD therapeutics that are rationally designed to function as multitargeted ligands to provide both symptomatic relief and demonstrate the disease-controlling effect [92, 175, 176]. Natural products such as ferulic acid (FA) have gained enormous interest in the development of therapeutic agents for many diseases, including AD [127, 133, 144, 147, 177-179]. FA (**Figure** 4.20) can be chemically identified as 4-hydroxy-3-methoxycinnamic acid and is naturally present in various plant species [31]. Apart from its antioxidant and anti-inflammatory activity, it also scavenges free radicals and inhibits Aβ aggregation. FA also showed inhibition properties against NLRP3 inflammasome [178, 180].

Our laboratory extensively develops novel ferulic acid template-based novel molecules targeting AD [147, 150, 174, 179, 180]. Earlier, we reported FA glycinamide derivatives **EJMC4a-4t** multifunctional ligands to target AD [147]. Given the piperazine ring's potential role in developing CNS active compounds[150-153], we also synthesized piperazine containing FA derivatives **EJMC-10a-10g [147]**. Intriguingly, piperazine-bearing molecules became weak inhibitors of AChE and BChE. We further carried out an SAR study by introducing a spacer between the phenyl ring and piperazine moiety located on the distal part of the earlier identified molecules (**EJMC-10a-10g**) to developed molecules **BMC-3a-3p** (AChE = 30 to 49 % and BChE = < 20 µM)[150]. Interestingly, the developed molecules

BMC-3l (BChE = 14.85 ± 0.37 μM) exhibited better inhibition properties towards BChE over **EJMC-10c** (BChE = 27.66 ± 0.39 %).

To further improve upon the multifunctional properties of FA-piperazine-based molecules and given the critical role played by the presence of the amide linker towards AChE inhibition in **EJMC-4a-4t** (AChE IC_{50} = 9 to 30 μM and BChE = 19 to 45 %), here we developed a novel series of molecules by introducing the amide linker between ferulic acid-piperazine and distal phenyl ring present in **EJMC-10c**. We started with the phenyl substitution and synthesized **18a-18m,** followed by an evaluation of cholinesterase inhibition activity. The **18a-18m** exhibited moderate to good activity against AChE. However, the developed molecules were weak inhibitors of BChE (Table 1). Given the well-tolerated behavior of quinoline towards AChE and BChE in **EJMC-7b** (IC_{50}, (μM) AChE, 4.89 ± 0.37, and BChE, 14.32 ± 0.04), we next replaced the distal phenyl ring with different positions of quinoline ring to develop **21a-21e**. The primary objective of replacing phenyl with quinoline was to target the more significant binding site of BChE [155]. It is noteworthy to observe the considerable improvement in BChE activity in the developed compound **21a-21e** (Table 1). Given the importance of metals in AD progression, our next goal was to introduce metal chelator, Aβ modulator, and antioxidant enhancer fragment. Earlier research has identified 8-hydroxy-quinoline (8-HQ) derivatives (**Figure** 4.20), such as clioquinol, PBT-1033, HLA-20, BMC-4g, and BMC-5b, as potential candidates for targeting metal chelation, regulating Aβ, and boosting antioxidant effects [156-159]. Therefore, we decided to replace the quinoline ring with an 8-HQ ring to synthesize **21f**. Intriguingly, **21f** was comparable to 5-amino-quinoline (5-AQ) towards AChE and BChE inhibition (Table 4.5). To further achieve improvement in AChE/BChE inhibitor property, based on our earlier observation of well-tolerated behavior of

the benzyl group present in **BMC-3a-3p** (IC_{50} < 20 µM), we decided to introduce 8-HQ benzyl moiety to synthesize **24a**. Interestingly, **24a** has shown promising activity toward cholinesterase enzyme with balanced activity towards AChE and BChE. The compound **24a** was further evaluated for enzyme kinetics study, PAS binding, metal chelation, inhibition of self-induced, and metal-induced Aβ aggregation. It was also assessed for cytotoxicity on PC12 cells, tested for NLRP3 inflammasome inhibition ability, and assessed for inhibition of mitochondrial ROS and total cellular ROS in a Drosophila model. We also evaluated **24a** in the scopolamine-induced amnesia model, followed by *ex-vivo* biochemical and neurochemical parameter estimation in this animal model.

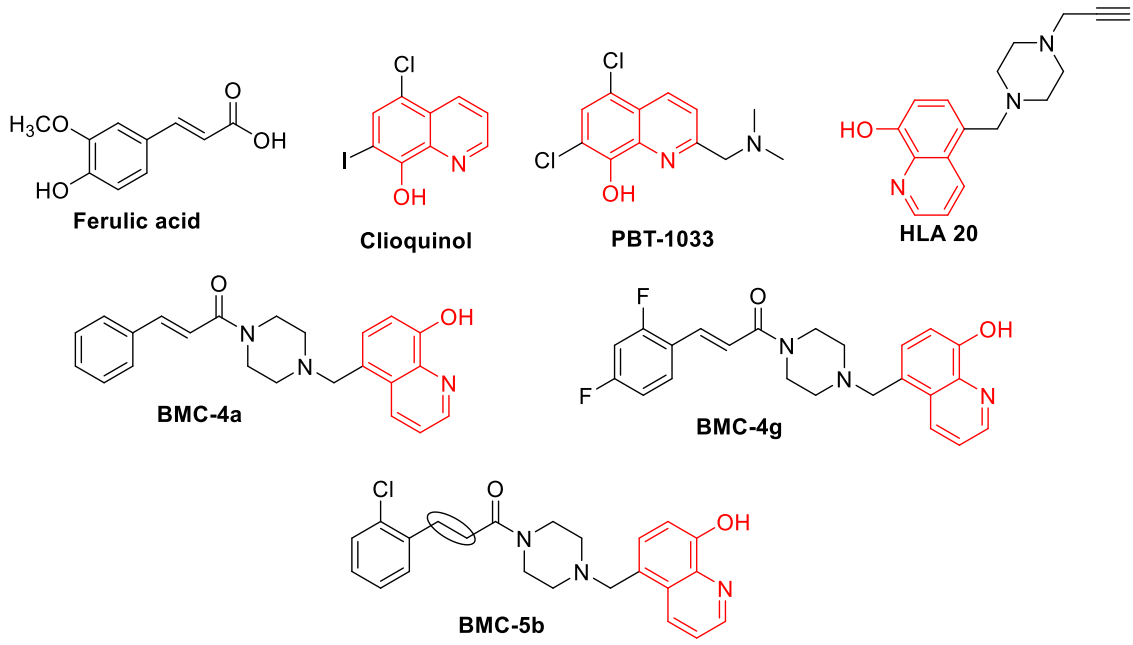

Figure 4.20: Ferulic acid and 8-hydroxyquinoline (8-HQ) derivatives [156-159].

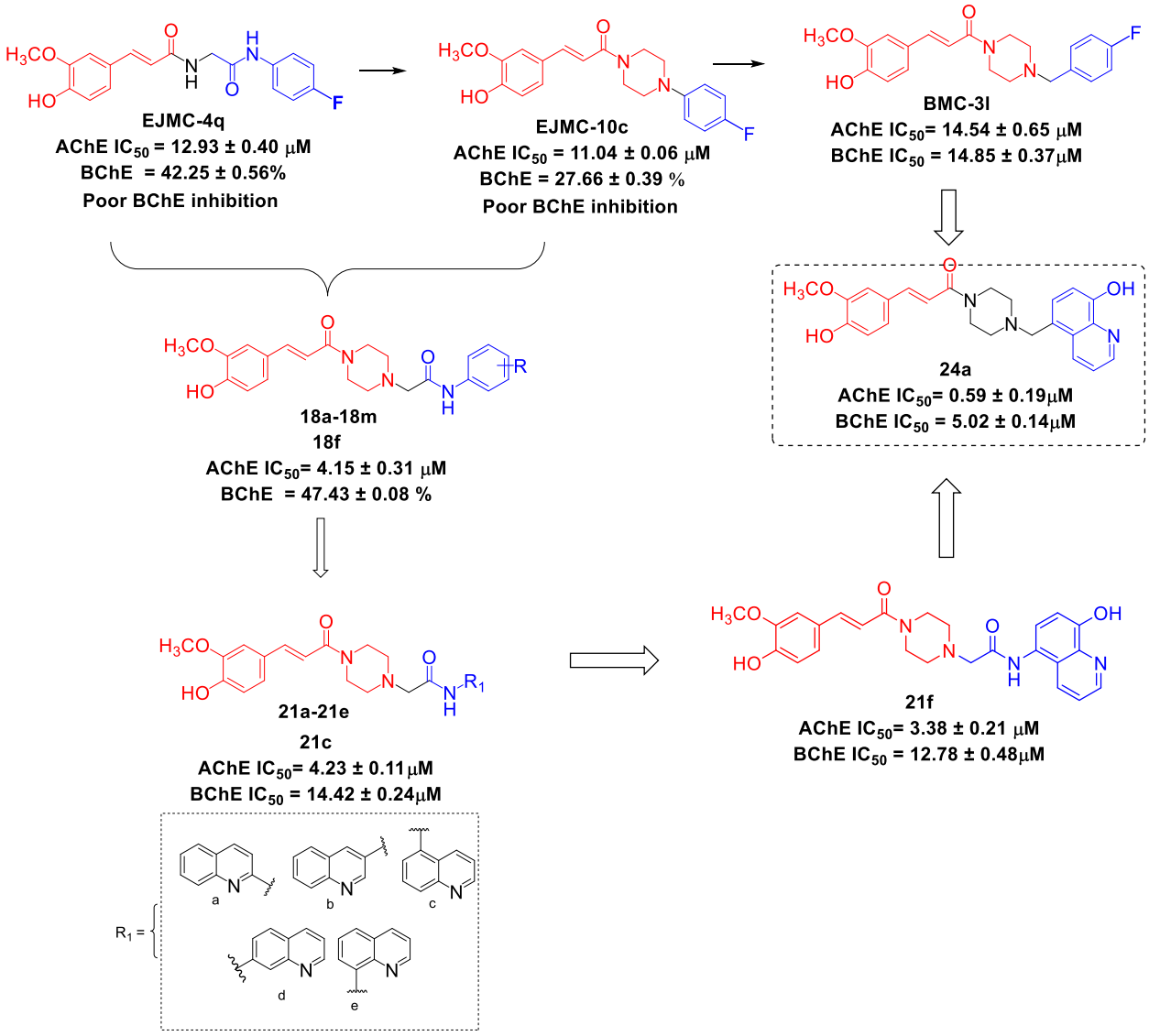

Figure 4.21: Lead-optimization pathway for ferulic acid-quinoline derivatives.

4.5 Chemistry involved in the second series (ferulic acid-piperazine acetamide) derivative

The synthesis of novel FA derivatives is depicted in Schemes **4-6**. Commercially available FA (**13**) underwent acid-amine coupling with boc-anhydride in the presence of EDC—HCl, HOBt, and triethylamine (TEA) to produce intermediate 14. Subsequently, boc-deprotection of 2 yielded intermediate **FAPIP** (**15**). Simultaneously, commercially available substituted anilines

(**16a-16m**) underwent a Schotten-Baumann reaction with chloroacetylchloride (6) to generate intermediates (**17a-17m**). These intermediates were then subjected to nucleophilic substitution reaction (SN2) with intermediate **FAPIP** (15), resulting in the synthesis of the final target compounds (**18a-18m**).

In scheme 2, various positional isomers of amino-quinolines (**19a-19f**) were treated with intermediate 4, resulting in the formation of intermediates **20a-20f** through a Schotten-Baumann reaction. After this, intermediates (**20a-20f**) participated in a nucleophilic substitution reaction (SN2) with intermediate FAPIP (**15**), ultimately leading to the synthesis of the final target compounds (**21a-21f**).

In Scheme 3, the 8-hydroxyquinoline (**22**) underwent chloromethylation to form 5-chloromethyl-8-hydroxyquinoline (**23**) using formaldehyde and HCl gas. Subsequently, it was subjected to a reaction with **FA-PIP** (**15**), providing acid-amine coupling conditions to yield the final product, **24a**.

4.6 Biological evaluation of the second series of compounds

4.6.1 *In-vitro* inhibition studies of *h*AChE and *eq*BChE

The depletion of acetylcholine (ACh) and other neurotransmitters in the brain has been identified as a significant factor in the advancement of AD. Clinically, extensive research supports the efficacy of cholinesterase inhibitors in ameliorating behavioral symptoms and decelerating cognitive deterioration in individuals diagnosed with AD. Therefore, we also screened our synthesized molecules against cholinesterase enzymes. The Ellman spectroscopic approach was used to assess the inhibitory effect of ferulic acid piperazine-acetamide`` derivatives against *h*AChE and *eq*BChE, and the results are expressed as IC_{50}, or the

concentration of inhibitor required to reduce the 50% activity of cholinesterase. [181]. FA was employed as the negative control, and **DPZ** was taken as a reference drug in this study.

First, we designed the FAPIP-phenylacetamide derivative, where a phenylacetamide fragment was attached with FA using a piperazine linker and synthesized compounds (**18a-18m**). Piperazine is a well-reported moiety that enhances solubility and rigidity in compounds, facilitating their binding to the active site of enzymes. We started our journey with FAPIP-phenylacetamide analogs and synthesized a compound **18a**. In *in-vitro* studies, **18a** exhibited moderate AChE inhibition activity with IC_{50}, (μM), AChE, **18a** = 18.02 ± 0.13), and weak BChE activity (% inhibition at 20 μM = 44.36 ± 0.25, table 1). Further, the methyl group was incorporated on *ortho, meta,* and *para*-positions of the phenyl ring situated on the distal position of **18a**. Compounds **18b-18d** (*ortho, meta,* and *para*) were designed and biologically evaluated for AChE/BChE inhibition study. In the enzyme inhibition study, **18c** was found to be most potent among **18b-18d** with IC_{50}, (μM), AChE, **18c** = 3.11 ± 0.35, and BChE % inhibition at 20 μM, 23.72 ± 0.21. Compounds **18b** and **18d** were found to be moderate inhibitors of *h*AChE and *eq*BChE with IC_{50}, (μM), AChE, **18b** = 15.13 ± 0.09 and **18d** = 14.43 ± 0.33 and BChE % inhibition at 20 μM, 18b = 45.01 ± 0.39 and **18d** = 34.02 ± 0.19 respectively. In the subsequent series of compounds, the phenyl ring **18a** was modified by incorporating ortho, meta, and para-methoxy and chloro functional groups, resulting in the synthesis of compounds **18e-18j**. In enzyme inhibition study, all the developed compounds (**18e-18j**) were moderate inhibitor of AChE and BChE with IC_{50}, (μM), AChE, **18e** = 19.54 ± 0.21, **18f** = 4.15 ± 0.31, **18g** = 18.07 ± 0.19, **18h**, 17.42 ± 0.27, 18**i** =15.25 ± 0.18 and **18j** = 18.14 ± 0.13 and BChE % inhibition at 20 μM, **18e** = 37.67 ± 0.13, **18f** = 47.43 ± 0.08, **18g** = 41.07 ± 0.34, **18h** = 19.32 ± 0.14 μM, **18i** =31.54 ± 0.19 and **18j =** 45.15 ± 0.03 (Table

4.5) respectively. We further incorporated bulky EWG in *ortho*, *meta*, and *para* positions of the terminal phenyl ring and developed compounds from **18k**, **18l,** and **18m**. Enzyme inhibition study revealed that bulky EWG was not well tolerated at the site of ChE as evident through enzyme inhibition studies and the developed compounds exhibited IC_{50}, (μM), AChE, **18k** = 16.45 ± 0.16, **18l** = 9.94 ± 0.31, **18m** = 17.24 ± 0.19 and BChE % inhibition at 20 μM, **18k** = 17.72 ± 0.09 μM, **18l** = 43.15 ± 0.27 and **18m** = 29.26 ± 0.32, respectively. Next, we incorporate a quinoline fragment instead of a phenyl ring to improve the designed molecules' anti-cholinesterase and antioxidant properties. We introduced a quinoline on different positions and synthesized compound **10a**-**10h** with IC_{50}, (μM), AChE, **21a** = 4.59 ± 0.17, **21b** = 7.36 ± 0.23, **21c** = 4.23 ± 0.11, **21d** = 9.74 ± 0.17, **21e** = 17.06 ± 0.28, **21f**=7.38 ± 0.21 and IC_{50}, (μM), BChE, **21a** = 18.41 ± 0.14, **21b** = 41.72 ± 0.17 %, **21c** = 14.42 ± 0.24, **21d** = 16.03 ± 0.7, **21e** = 37.03 ± 0.41 %, **21f** = 12.78 ± 0.48 respectively (Table 4.5). We slightly modified the structure of **21f** and synthesized compound **24a**. Interestingly, compound **24a** was identified as the most potent cholinesterase inhibitor among all synthesized molecules, exhibiting IC_{50} (μM), AChE, 0.59 ± 0.19, BChE, 5.02 ± 0.14. Therefore, we selected **24a** for further *in-vitro* and *ex-vivo* evaluation.

Table 4.5. Cholinesterase inhibitory activities of the developed derivatives.

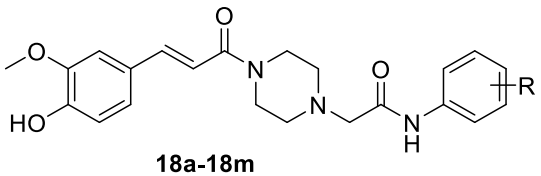

18a-18m

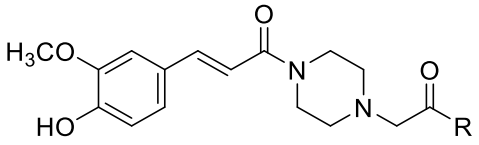

21a-21f

SN	Code	R	AChE IC_{50} or %inhibition @ 20 µM	BChE IC_{50} or % inhibition @ 20 µM
1	**18a**	hydrogen	18.02 ± 0.13	44.36 ± 0.25 %
2	**18b**	o-toluidine	15.13 ± 0.09	45.01 ± 0.39%
3	**18c**	m-toluidine	3.11 ± 0.35	47.72 ± 0.21 %
4	**18d**	p-toluidine	14.43 ± 0.33	34.02 ± 0.19 %
5	**18e**	o-anisidine	19.54 ± 0.21	37.67 ± 0.13%
6	**18f**	m-anisidine	4.15 ± 0.31	47.43 ± 0.08 %
7	**18g**	p-anisidine	18.07 ± 0.19	41.07 ± 0.34 %
8	**18h**	o-chloro	17.42 ± 0.27	19.32 ± 0.14 µM
9	**18i**	m-chloro	15.25 ± 0.18	31.54 ± 0.19 %
10	**18j**	p-chloro	18.14 ± 0.13	45.15 ± 0.03 %
11	**18k**	o-trifluoromethyl	16.45 ± 0.16	17.72 ± 0.09 µM
12	**18l**	m-trifluoromethyl	9.94 ± 0.31	43.15 ± 0.27 %
13	**18m**	p-trifluoromethyl	17.24 ± 0.19	29.26 ± 0.32
14	**21a**	2-aminoquinoline	4.59 ± 0.17	18.41 ± 0.14 µM
15	**21b**	3-aminoquinoline	7.36 ± 0.23	41.72 ± 0.17 %
16	**21c**	5-aminoquinoline	4.23 ± 0.11	14.42 ± 0.24 µM

17	**21d**	7-aminoquinoline	9.74 ± 0.17	16.03 ± 0.7 μM
18	**21e**	8-aminoquinoline	17.06 ± 0.28	37.03 ± 0.41 %
19	**21f**	5-amino-8hdroxy-quinoline	7.38 ± 0.21	12.78 ± 0.48
20	**24a**	5-amino-8hdroxy-quinoline	0.59 ± 0.19	5.02 ± 0.14 μM

IC_{50} = 50% inhibitory concentration (means ± SD of 3 independent experiments)

inhibition was determined at 20μM inhibitor concentration (in triplicate)

4.6.2 Determination of enzyme kinetics of 24a against AChE/BChE

Enzyme kinetics analysis used Lineweaver-Burk plots to understand how potent cholinesterase inhibitor **24a** inhibits the enzyme. The Lineweaver-Burk reciprocal plot (**Figure 4.22**) is widely used for analyzing enzyme kinetics data. It involves plotting the reciprocal of the initial enzyme reaction velocity (1/V) against the reciprocal of the substrate concentration (1/[S]). In this experiment, reciprocal plots of substrate concentration versus velocity were generated by adding varying concentrations of **24a** (10, 5, and 1 μM) for AChE and (30, 15, and 7.5 μM) for BChE in the presence of different substrate (ATCI/BTCI) concentrations (0.5, 1.0, 1.5, 2.0 and 2.5 μM). The results indicate that compound **24a** demonstrates a mixed-type inhibition mechanism against both *h*AChE and *eq*BChE, involving binding to both the enzyme and the enzyme-substrate complex, leading to a reduced reaction rate.

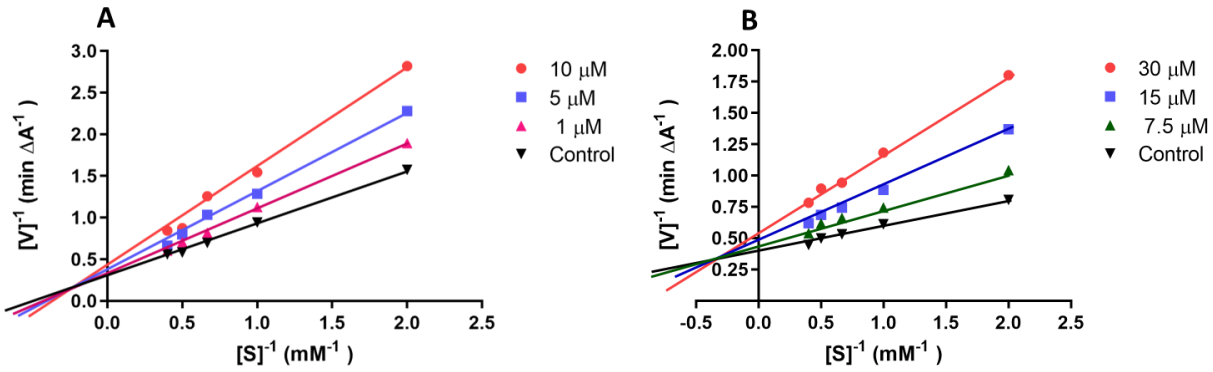

Figure 4.22: Lineweaver-Burk plot represents the mechanism of *h*AChE and *eq*BChE inhibition. A) Lineweaver-Burk plots for *h*AChE at 1, 5, and 10 µM concentration of **24a** with varying acetylthiocholine concentration (. B) Lineweaver-Burk plots for *eq*BChE at 7.5, 15, and 30 µM of **24a** with increasing butyrylthiocholine concentrations. The lines represent data analyzed through weighted least-squares; results are reported as means of two independent experiments ± standard deviation.

4.6.3 Determination of antioxidant activity of 24a through DPPH radical scavenging assay

The DPPH method is a widely used and cost-effective technique for evaluating antioxidant properties by measuring the ability of substances to act as hydrogen providers or free-radical scavengers. Upon reaction with a free-radical scavenging antioxidant, DPPH decolorizes, indicating the reduction in electron absorption and highlighting the substance's antioxidant capacity. It is noteworthy that **24a** and 21**f** exhibited the highest activity in the DPPH assay (**Figure 4.23**), demonstrating IC_{50} values of 5.88 ± 0.21 µM and 4.33 ± 0.19 µM (Table 4.6), respectively. Recognizing the vital role of antioxidants in combatting free radicals and ROS, based on enzyme inhibition and antioxidant potential, we further investigated **24a** potential in countering H_2O_2-induced oxidative stress in the PC12 cell line, modulating the release of ROS

in human microglial cells. The remaining compounds displayed moderate activity within the 34 to 55 µM range, as outlined in **Table 4.6**.

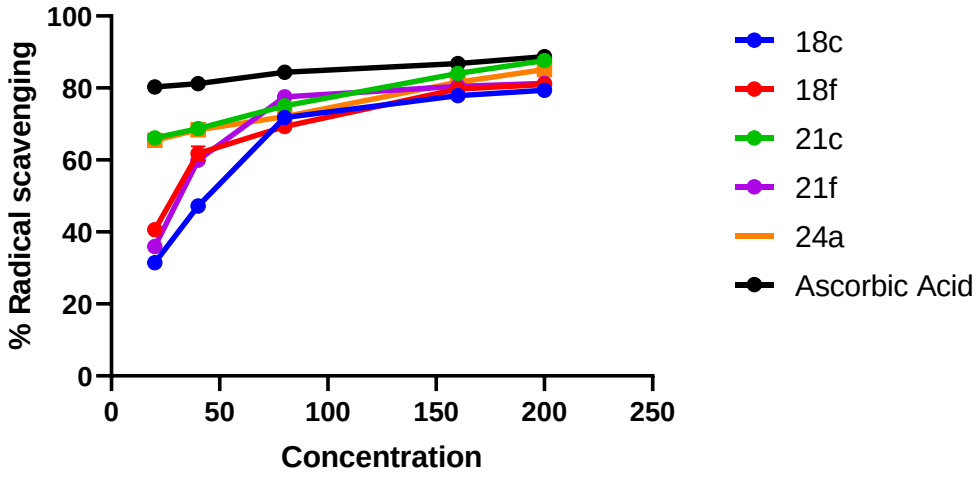

Figure 4.23: Antioxidant activity graph plot of compound 18c, 18f, 21c, 12f, **24a** and ascorbic acid.

Table 4.6: Antioxidant assay (DPPH assay) of 18c, 18f, 21c, 21f, 24a and ascorbic acid

S.No.	Code	% radical scavenging	IC_{50} (µM)[b]
1	18c	40.60 ± 0.91	49.54 ± 0.27
2	18f	31.48 ± 0.64	34.65 ± 0.31
4	21c	35.93 ± 0.06	39.43 ± 0.13
3	21f	66.07 ± 0.62	4.33 ± 0.19
5	**24a**	65.45 ± 0.11	5.88 ± 0.21
6	Ascorbic acid	81.03 ± 0.14	2.42 ± 0.31

[a] Determines % radical scavenging @ 20 µM.

[b] Determines the concentration required to inhibit 50%

The result is presented as the mean ± SD of the experiments conducted in duplicate.

4.6.4 In-silico studies with compound 24a

4.6.4.1 Molecular docking study of 24a against AChE and BChE

Compound **24a** demonstrated effective inhibition against both AChE and BChE in laboratory studies. Therefore, we decided to select **24a** for *in-silico* studies. Molecular modeling analysis highlighted significant interactions with AChE (PDB # 4EY7), such as a π-alkyl interaction with Tyr72 and hydrogen bonding with Tyr341. Additionally, it engaged in π-π interactions and π-sigma interactions with Trp86 and Trp286, respectively. The binding affinity with AChE was found to be -11.9 kcal/mol. For BChE (PDB # 4BDS), **24a** formed conventional hydrogen bonds with Ala150, His438 and Ser198, π-π stacking with Phe329, and Trp231 (**Figure 4.24**). **24a** showed alkyl interactions with Leu273 and Val288. However, less favorable interactions resulted in a reduced binding affinity (-9.3 kcal/mol) with BChE. The molecular docking outcomes mimic the *in-vitro* findings, providing insight into well-balanced activity through specific interactions at the active sites of both enzymes.

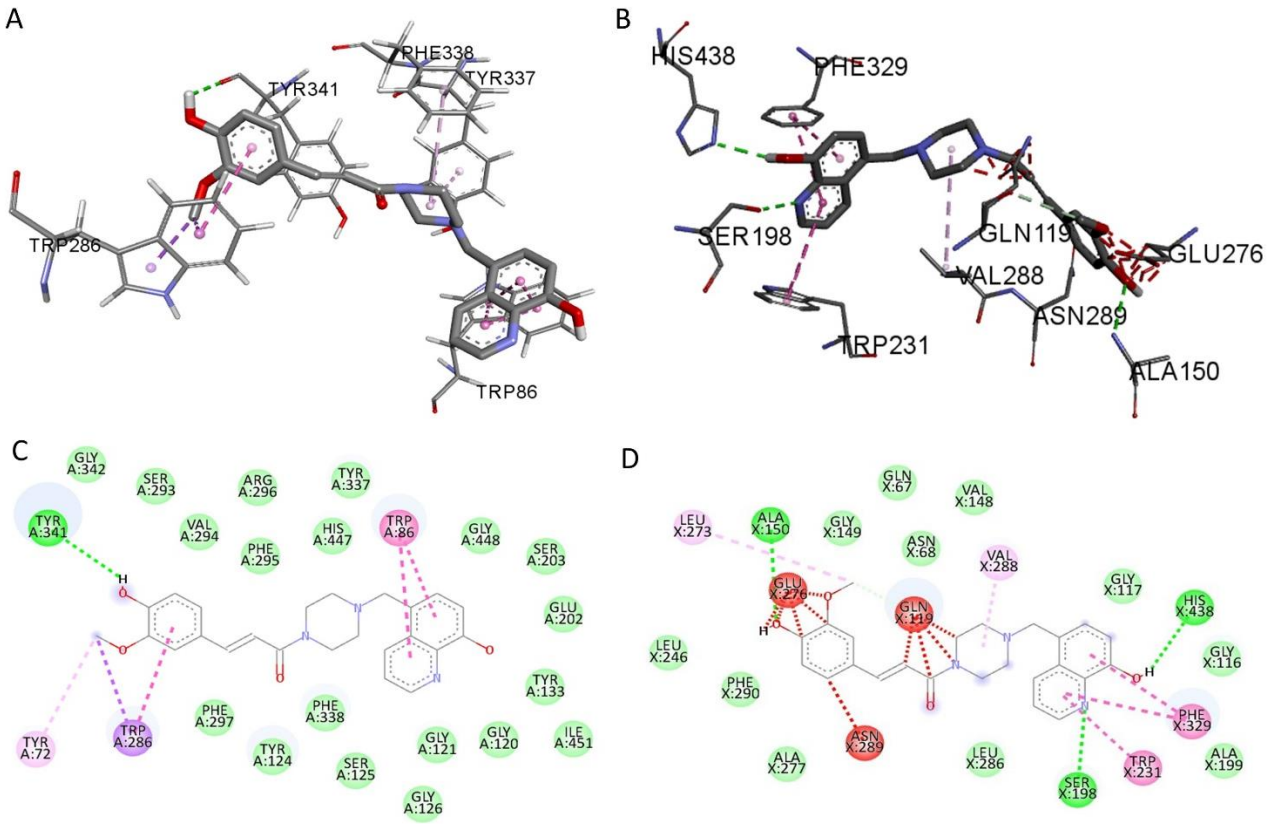

Figure 4.24: Molecular docking study of **24a**. A and B illustrate the 3D interaction diagram of compound **24a** with the acetylcholinesterase protein (4EY7) and butyrylcholinesterase protein (4BDS), respectively. On the other hand, C and D depict the 2D interaction diagram of **24a** with 4EY7 and 4BDS.

4.6.4.2 Molecular dynamics studies of 24a against AChE and BChE

The docking-predicted binding modes of **24a** with acetylcholinesterase (AChE, 4EY7) and butyrylcholinesterase (BChE, 4BDS) proteins underwent molecular dynamics simulations to delve into essential interactions, three-dimensional conformational changes, and stability over a 100 ns duration. The simulated system's root mean square deviation (RMSD) was tracked, revealing stable protein structures for 4EY7 and 4BDS throughout the 100 ns simulation.

Specifically, 4EY7 exhibited minimal deviation (RMSD: 0.19-0.27 nm), while **24a** initially displayed deviation against 4EY7 (RMSD: 0.32-0.70 nm) (**Figure 4.25 A**) but achieved stability by 100 ns. This deviation, attributed to the inherent flexibility of small molecules, underscores their dynamic changes during initial interactions with proteins, allowing optimal binding poses. In contrast, 4BDS exhibited RMSD in the range of 0.27-0.33 nm, while **24a** displayed deviation (RMSD: 0.28-0.69 nm) initially, stabilized after 60 ns (**Figure 4.25 E**). This aligns with *in-vitro* enzyme activity, reflecting **24a** decreased activity against BChE compared to AChE. Subsequently, root mean square fluctuations (RMSFs) were analyzed, indicating minimal core fluctuation (0.05-0.55 nm for 4EY7, 0.05-0.56 nm for 4BDS, **Figure 4.25 B** & **F**). C- and N-termini of 4EY7 and 4BDS exhibited higher RMSF consistent with solvent exposure. **24a** demonstrated narrow fluctuation against 4EY7 (RMSF: 0.02-0.17 nm) and 4BDS (RMSF: 0.03-0.27 nm), suggesting better binding to 4EY7 (**Figure 4.25 C** & **G**). Radius of gyration (Rg) analysis emphasized stable three-dimensional proportions for 4EY7-**24a** (Rg: 2.285-2.345 nm) and 4BDS-**24a** (Rg: 2.305-2.375 nm) (**Figure 4.25 D** & **H**), indicating maintained compactness without sudden expansion. This Rg parameter is crucial for understanding structure-activity relationships in ligand-protein complexes.

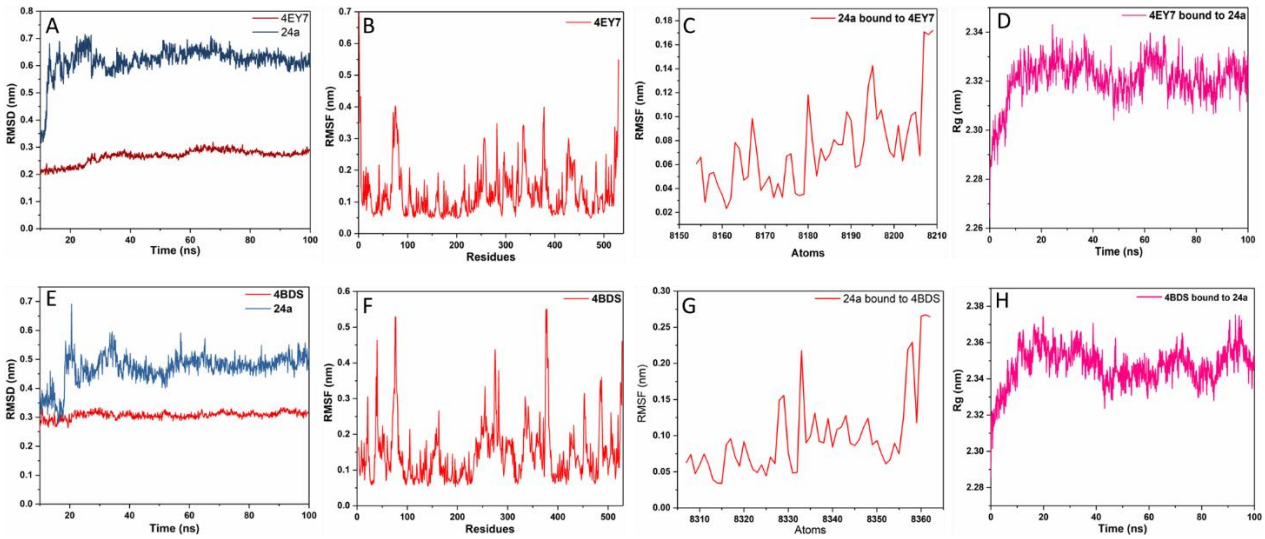

Figure 4.25: The molecular dynamics studies of compound **24a** against 4EY7 (AChE) and 4BDS (BChE). A) The root mean square deviation (RMSD) plot of **24a** against 4EY7. B) The root mean square fluctuation (RMSF) of protein 4EY7. C) RMSF plot of **24a** against 4EY7. D) Radius of gyration plot of **24a** against 4EY7. E) The root mean square deviation (RMSD) plot of **24a** against 4BDS. F) The root mean square fluctuation (RMSF) of protein4BDS. G) RMSF plot of **24a** against 4BDS. H) Radius of gyration plot of **24a** against 4BDS.

4.6.5 Evaluation of PAS binding activity through propidium iodide displacement assay

The study examined how compound **24a** impacts the peripheral active site (PAS) of acetylcholinesterase (AChE), an enzyme crucial for controlling neurotransmission. In our investigation, we employed a competitive displacement experiment using propidium iodide to assess the binding affinity **24a** against the PAS site of AChE. We measured changes in fluorescence intensity when AChE was incubated with different concentrations of compounds **24a**, **FA, or DPZ** (at 5, 10, 20, and 50 μM) in combination with propidium iodide, as presented in **Table 4.7**. The data indicated that **24a** effectively displaced propidium iodide, with a displacement value of 23.60 ± 0.14 (table 4.7), comparable to the reference drug **DPZ** (25.08

± 0.34). These findings suggest that **24a** has the potential to efficiently bind to the PAS site of AChE, making it a promising therapeutic strategy for regulating neurotransmission.

Table. 4.7. Evaluation of Propidium Iodide Displacement from the Peripheral Anionic Site (PAS) of AChE by 24a, FA, and DPZ

Code	5 μM	10 μM	20 μM	50 μM
24a	13.87 ± 0.12	15.50 ± 0.27	20.70 ± 0.31	23.60 ± 0.14
FA	0.12 ± 0.35	2.22 ± 0.37	5.10 ± 0.19	8.65 ± 0.25
DPZ	15.23 ± 0.09	16.75 ± 0.19	23.88 ± 0.29	25.08 ± 0.34

Results are reported in mean ± SD for two independent experiments.

4.6.6 Measurement of metal-chelating properties of 24a

Compound **24a**, which has shown the most notable enzyme inhibition and antioxidant properties, was chosen to assess its ability to chelate metal ions. The dysregulation of certain biometals, particularly iron, is a critical factor in AD progression, as its accumulation in the extracellular space induces oxidative stress, highlighting the potential of targeting biometal dysregulation as a therapeutic strategy for AD. A UV-visible spectroscopy assay was employed to evaluate the metal chelation capacity of compound **24a** (as depicted in **Figure** 4.26). The experimental procedure involved mixing equal concentrations of **24a** and $FeCl_3 \cdot 6H_2O$, followed by a comprehensive analysis of the resulting complex formation. In **Figure 4.26 A**, the absorption spectra of compound **24a**, both alone and in the presence of FeCl3·6H2O, displayed significant differences. Specifically, at pH 7.4 and in the presence of Fe3+, the

spectra exhibited increased intensity around 480 nm compared to lower pH levels (4.2), providing conclusive evidence of complex formation between **24a** and Fe3+. The interaction between **24a** and Fe^{3+} was further investigated by gradually adding $FeCl_3 \cdot 6H_2O$ to **24a** in different molar ratios, as shown in **Figure 4.26 B**, and changes in absorption at 511 nm were monitored. Subsequently, the absorbance values were plotted about the mole fraction of **24a**. An isosbestic point at nearly 6.75 in **Figure 4.26 C** signifies a stoichiometry of 2:1 for the complex established between **24a** and Fe3+.

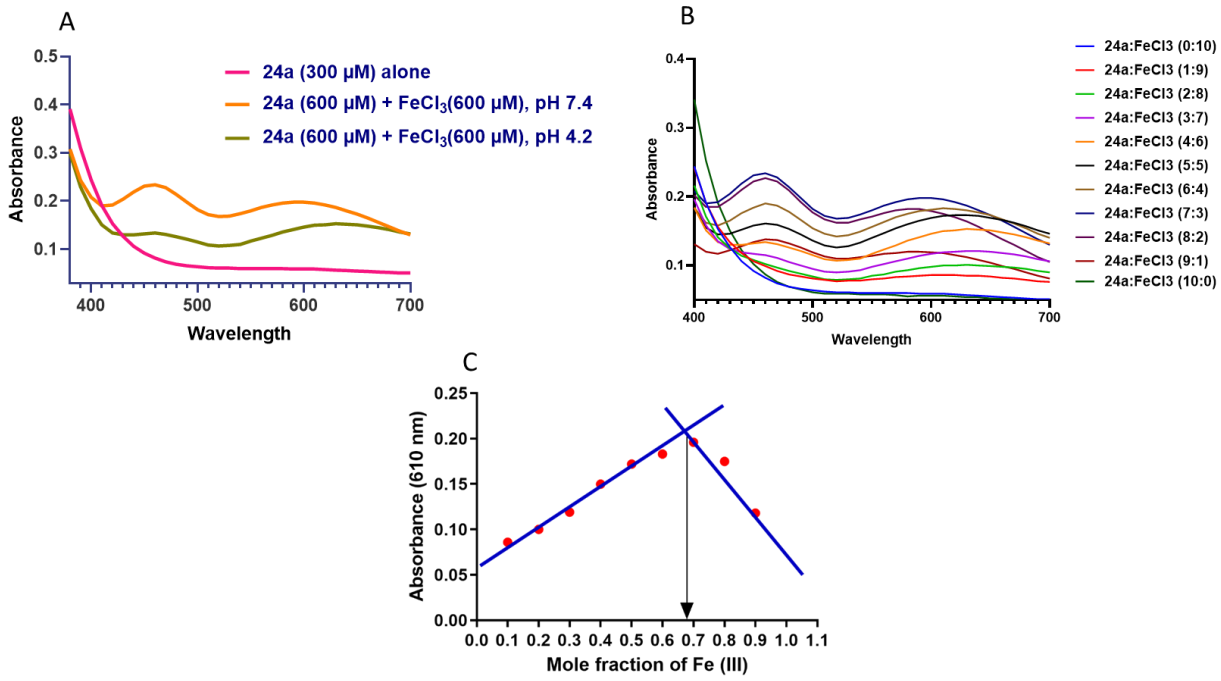

Figure 4.26: Metal chelating effect of **24a**. (**A**) UV absorbance spectrum of compound **24a** (300 μM) alone or with $FeCl_3$ (300 μM) in extrapure methanol. B) Determining the stoichiometry of the **24a**–Fe^{3+} complex through the molar ratio method. (C) Job's plot for compound **24a** against Fe (III).

4.6.7 Inhibition of self and metal-induced Aβ$_{1-42}$ aggregation by 24a

To determine the inhibition properties of compound **24a** against self-induced and metal-induced Aβ$_{1-42}$ aggregation, we utilize Thioflavin T (ThT) fluorescence assay. The ThT fluorescence assay is a proven method for detecting amyloid fibrils, offering crucial insights into the structure and formation mechanisms of these fibrils associated with severe human diseases like Alzheimer's and Parkinson's [182, 183]. Metal ions, specifically Cu2+ and Fe3+, are known to induce the aggregation of Aβ$_{1-42}$. The data presented in **Figure 4.27** clearly illustrate that **24a** exhibits a substantial inhibitory influence on the aggregation of Aβ$_{1-42}$. The inhibitory impact of **24a** on metal-induced Aβ aggregation revealed its dual role in countering self-induced and metal-induced Aβ aggregation processes. In summary, the results outlined above provide valuable insights into the potential utility of **24a** as a preventive intervention for AD.

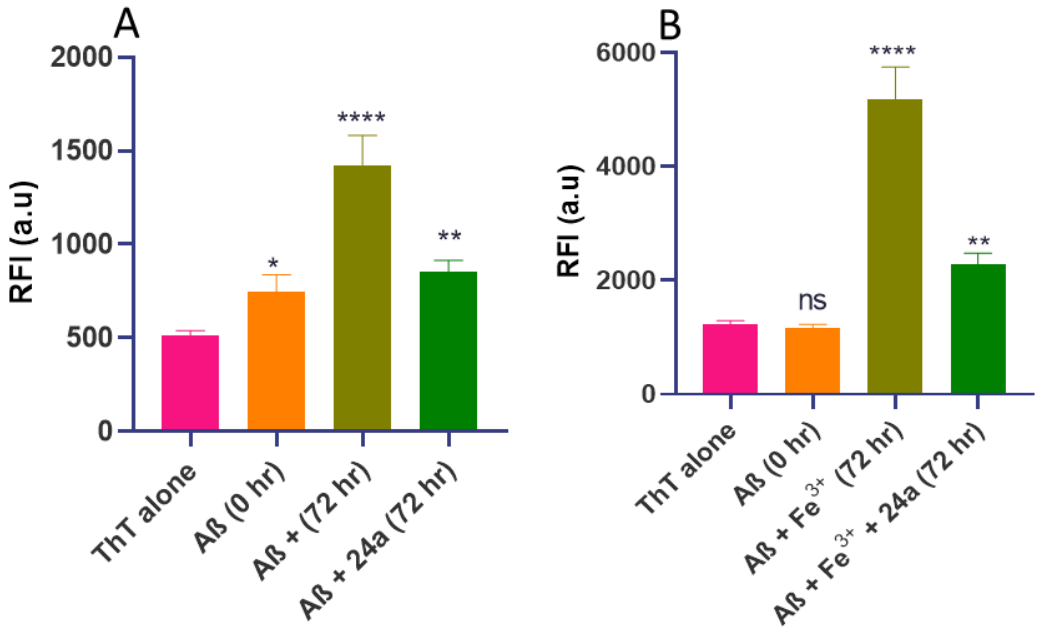

Figure 4.27: The inhibitory impact of compound **24a** on Aβ aggregation was assessed in two scenarios. (A) Aβ$_{1-42}$ self-aggregation and (B) iron-induced Aβ$_{1-42}$ aggregation. Aβ$_{1-42}$ (12.5

μM) was incubated alone, with **24a** (6.25 μM) or **24a** + Fe^{3+} for 72 hours, followed by ThT assay. Statistical significance is denoted by * for $p < 0.05$, ** for $p < 0.01$, *** for $p < 0.001$, **** for $p < 0.0001$, and "ns" for $p > 0.05$. The data is the mean ± standard error derived from two independent experiments.

4.6.8 Cell cytotoxicity assay of compound 24a on PC12 cells.

The cell cytotoxicity study was conducted in **Dr. Saroj Kumar's** laboratory, and Sanskriti Rai performed experiments. The MTT (3-(4,5-dimethylthiazol-2-yl)-2,5-diphenyltetrazolium bromide) assay was carried out to assess the cytotoxic effects of compound **24a** on the viability of PC12 cells. PC12 cells are widely utilized as an ideal cellular model for examining novel drug candidates for AD. Previous research has indicated that upon differentiation, PC12 cells closely mimic neurons in terms of morphology, physiology, and biochemical functions [184]. Therefore, all experiments in this study were conducted using differentiated PC12 cells. Before *in-vivo* studies, *in-vitro* cytotoxicity investigations were necessary. The **24a** possesses potent antioxidant and metal chelation properties and inhibitory activity against AChE/BChE and was selected for cytotoxicity assessment on the PC12 cell line. After 24 hours of treatment with various concentrations (1-30 μM) of **24a**, PC12 cells exhibited no significant toxicity (**Figure 4.28**), indicating a favorable safety profile up to 30 μM, the highest concentration tested.

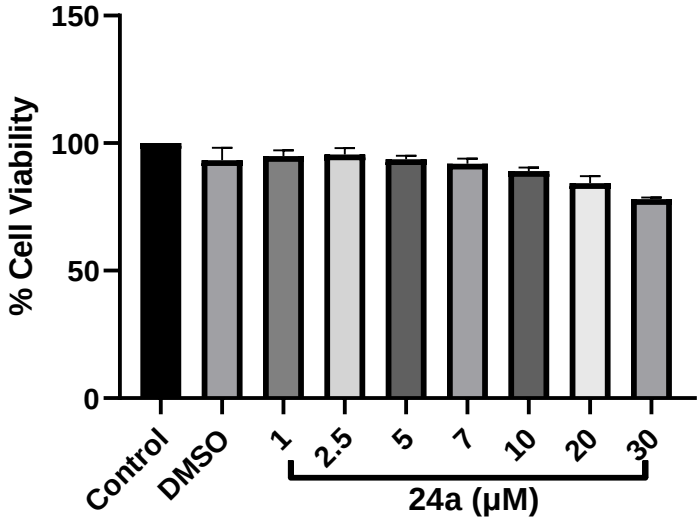

Figure 4.28: The effect of **24a** on cellular viability was investigated by exposing cells to varying concentrations of **24a** (1, 2.5, 5, 7, 10, 20, and 30 µM) for 24 hours. Cell viability, as a percentage, was assessed using the MTT assay. Results, based on quadruplicate samples, are presented as mean ± SE.

4.6.9 Evaluation of *In-vitro* blood-brain barrier permeability of 24a using PAMPA assay

We examined the ability of potential ferulic acid-quinoline derivatives to enter the brain by using a parallel artificial membrane permeation (PAMPA) assay. The PAMPA serves as a screening method to assess the permeability of drugs across the blood-brain barrier, utilizing a microplate format. In PAMPA, a drug candidate is permitted to penetrate the lipid layer of a specific well over an incubation period, typically ranging from 10 to 16 hours. To validate the assay, we compared experimental permeability values with reported values for commercially available drugs like imipramine (positive control) and hydrocortisone (negative control), as established by Di et al. Compounds with permeability values surpassing 4.8×10^{-6} cm s^{-1} were considered capable of passive diffusion through the blood-brain barrier. The findings revealed

that compound **24a** exhibited permeability values (5.96 ± 0.13 × 10^{-6} cm s^{-1}, **table 4.8**) exceeding this threshold, indicating their potential to cross the BBB effectively. This suggests promising prospects for their ability to access the central nervous system.

Table 4.8: PAMPA-BBB assay for **24a**, imipramine and hydrocortisone

S.No.	Compound	P_e (exp)[a]	Literature value[b]	Experimental observation
1	**24a**	5.96 ± 0.13	-------	CNS (+)
2	Imipramine	14.06 ± 0.27	13.0	CNS (+)
3	Hydrocortisone	0.21 ± 0.03	0.19	CNS (-)

Pe Represents Permeability (P_e = 10^{-6} cm s^{-1})

[a] Represents the average (mean) ± SD of two independent experiments.

[b] Represents literature value [168].

[c] CNS (+) defines high permeability with Pe > 4.0, CNS (-) indicates low permeability with Pe < 2.0, and CNS (±) signifies uncertain permeability within the range of 2.0 to 4.0.

4.6.10 Evaluation of 24a in NLRP3 Model

The NLRP3-related experiments were conducted in **Dr. VGM Naidu's** laboratory, and **Samir Kumar Panda** performed the experiments.

4.6.10.1 Effect of 24a on proliferation and cytotoxicity caused by LPS and ATP co-treatment.

The detailed experimental timeline for *in-vitro* experiments is described in **Figure 4.29 A**. Compound **24a** treatment at a dose of 5 and 10µM exhibits a significant increase in the microglial cell proliferation when compared to LPS and ATP exposed group **(Figure 4.29B, C)**. The results suggest the strong anti-inflammatory nature of the compound and its potential to halt NLRP3 inflammasome-mediated microglial cell death.

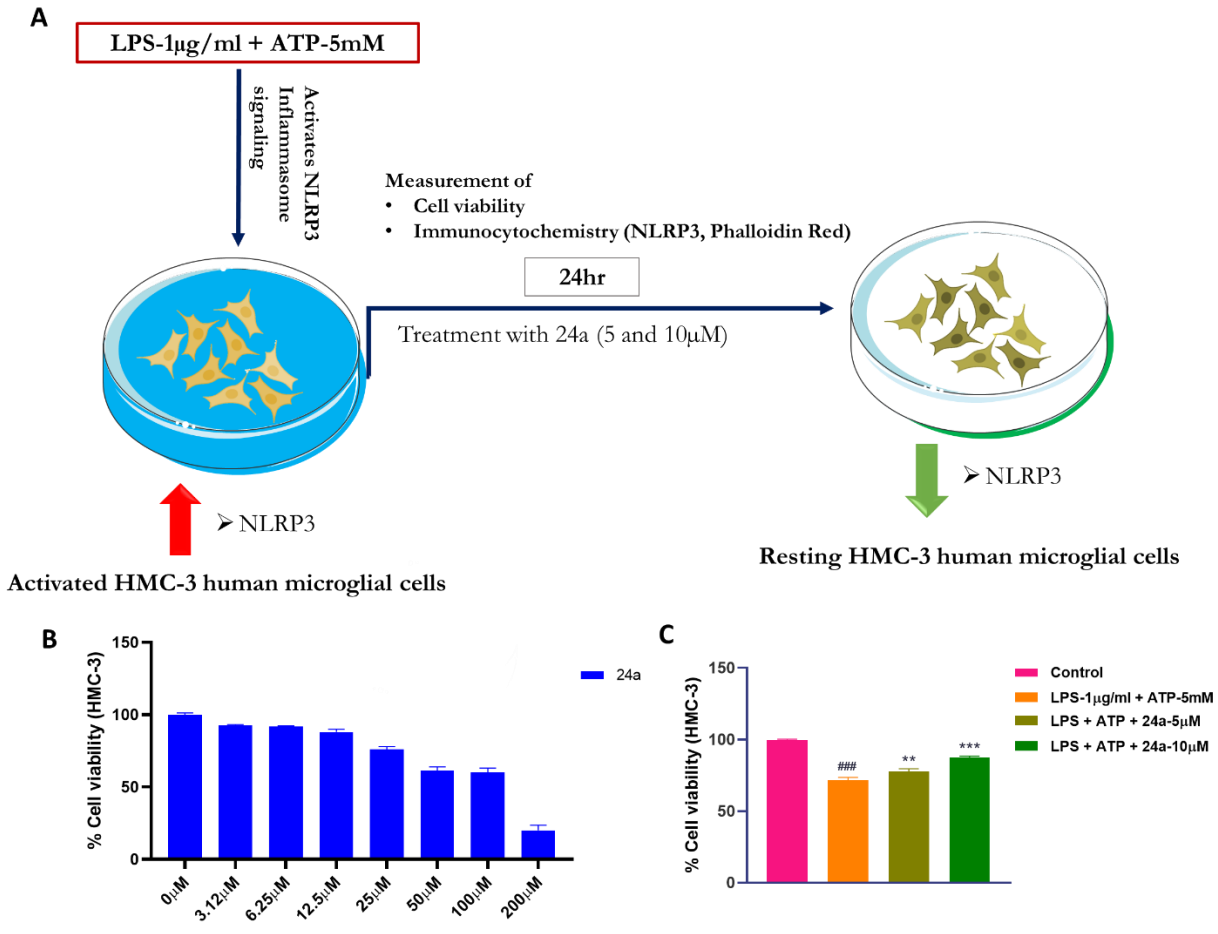

Figure 4.29: Compound **24a** exhibits significant inhibition in the microglia toxicity caused due to LPS and ATP induction. A) Graphical representation depicting the *in-vitro* experimental

design. B) Treatment with **24a** at varying doses to identify the proliferative and non-toxic dose. C) To check the proliferative effect of compounds against NLRP3 inflammasome-mediated inflammation, HMC-3 cells were primed with LPS (1µg/ml) and ATP (5 mM). Further cells were treated with the test compound **24a** at a dose of 5 and 10µM. Compound **24a** showed a significant increase in microglial proliferation compared to the LPS+ATP-treated group. All the data were analyzed as mean ± SD (n = 3). Statistical significance was further determined by one-way ANOVA followed by Tukey's test in which the LPS+ATP group was compared with the control, where statistical significance was defined as #$p<0.05$, ##$p<0.01$, and ###$p<0.001$, and *$p<0.05$, **$p<0.01$, and ***$p<0.001$ represent LPS+ATP vs **24a** respectively.

4.6.10.2 Effect of 24a on NLRP3 signaling cascade and microglial activation in HMC-3 cells.

Recent studies have demonstrated the critical function NLRP3 inflammasome inhibitors play via NLRP3 in managing neurodegenerative disorders. Since neuroinflammation and neurodegeneration are strongly related, targeting NLRP3 inflammasome activation may be a sensible tactic to combat AD pathogenesis. Treatment with compound **24a** at a dose of 5 and 10µM showed a marked reduction in the expression levels of NLRP3 **(Figure 4.30 A, B)**, suggesting its anti-inflammatory and anti-microglial activation effects. The compounds were further effective in inhibiting microglial activation.

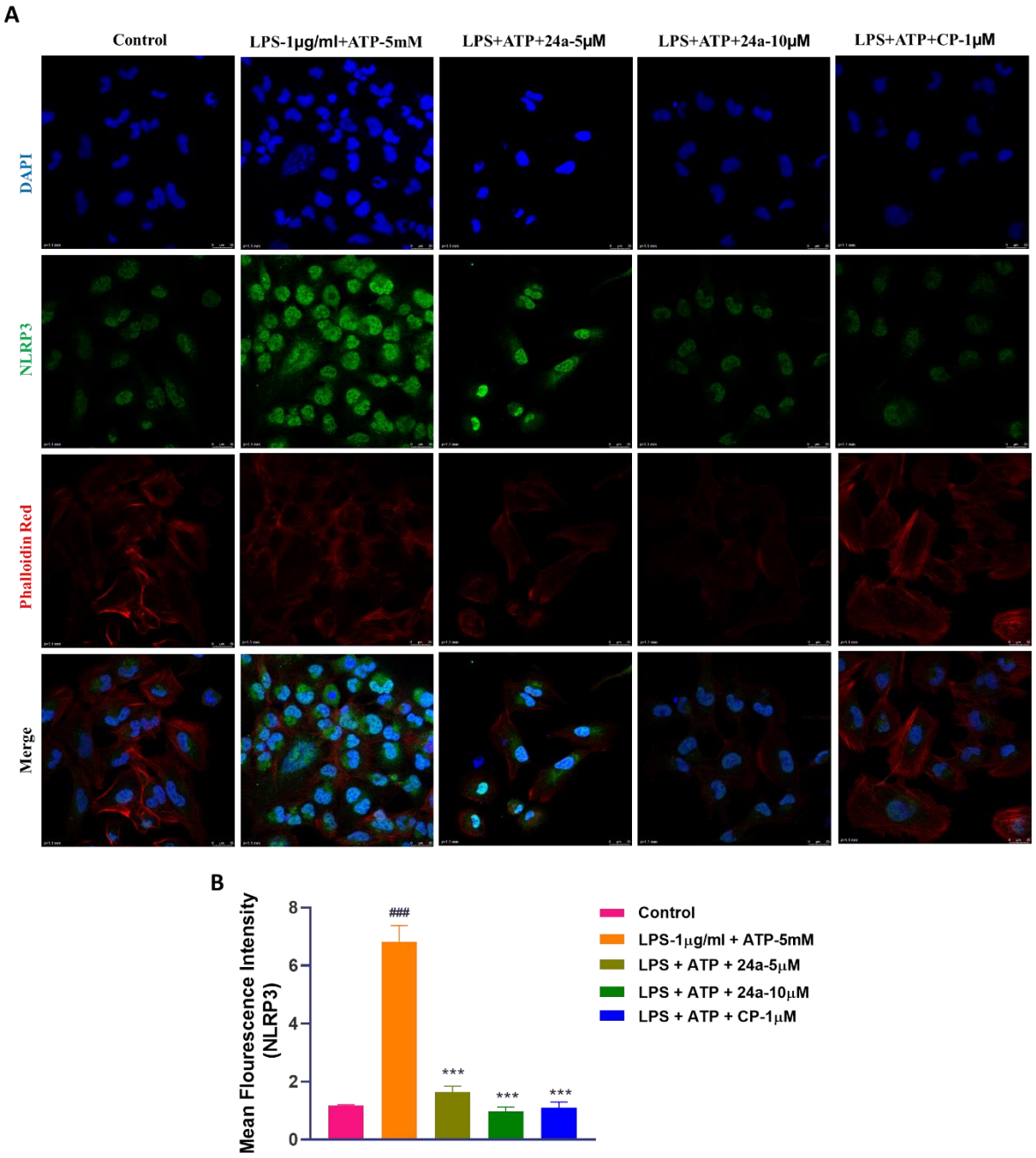

Figure 4.30: Compound **24a** inhibited microglial activation and reduced the NLRP3 inflammasome activation as evidenced by Immunocytochemistry (ICC) staining of HMC-3 cells for NLRP3 and Phalloidin Red. A) HMC-3 cells stained with DAPI (nuclear stain), NLRP3 (Green), and Phalloidin red (Red) to assess NLRP3 inflammasome expression and

microglial activation. B) Bar graph representing the Mean Fluorescence intensity of NLRP3. All the data were analyzed as mean ± SD (n=3). Statistical significance was further determined by one-way ANOVA followed by Tukey's test in which the LPS+ATP group was compared with the control, where statistical significance was defined as #p<0.05, ##p<0.01, and ###p<0.001, and *p<0.05, **p<0.01, and ***p<0.001 represent LPS+ATP vs **24a** respectively.

4.6.11 Evaluation of compound 24a in transgenic drosophila model of AD.

The Drosophila-related experiments were conducted in **Dr. S. Srikrishna's laboratory**, and **Prabhat Kumar** performed the experiments. I also partially contributed to these experiments.

4.6.11.1 Therapeutic efficacy of 24a and DPZ on OregonR+ an AD model of Drosophila

Various concentrations of **24a** and **DPZ** drugs were administered to OregonR+ flies to determine the median lethal dose (LD50). OregonR+ flies grown on standard food did not show lethality, with 100% eclosed flies. Flies raised in **24a** at concentrations of 0.05 and 0.1 mg/ml exhibited 98% and 97% eclosed flies, respectively, while the 0.2 mg/ml concentration resulted in approximately 82% eclosed flies [**Figure 4.31 A**]. Therefore, **24a** at 0.05 and 0.1 mg/ml showed no toxicity toward fly development, recommended for future application against AD. Similarly, the reference drug **DPZ** showed a 90% eclosed fly rate at 100 µM/ml concentration. However, at higher concentrations of 200 µM/ml, 400 µM/ml, and 800 µM/ml, **DPZ** exhibited approximately 55%, 38%, and 35% eclosed flies, respectively [**Figure 4.31B**]. Consequently, **DPZ** demonstrated lower toxicity at 100 µM/ml, so this concentration of **DPZ** was considered for further studies.

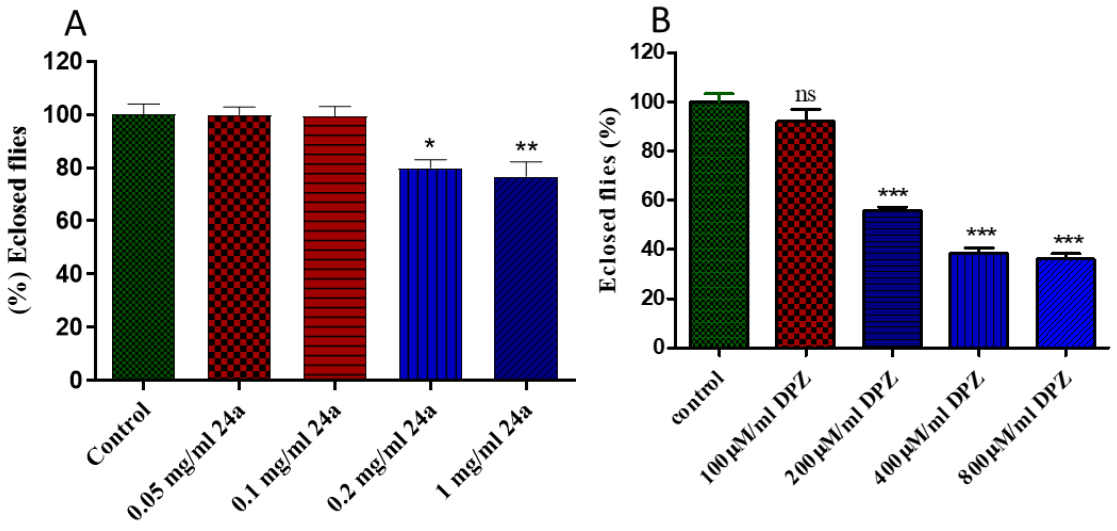

Figure 4.31: The toxicity studies of compound **24a** and **DPZ** in the Drosophila model. A) Toxicity studies of compound **24a** at different concentrations (0.05, 0.1, 0.2, and 1 mg/ml). B) Toxicity studies of standard donepezil at different concentrations (100, 200, 400, and 800 µM). Statistical analysis was performed using one-way ANOVA followed by the Dunnet test, where ns were not significant, **p<0.01, *** p<0.001, **** p<0.0001 compared to the control group.

4.6.11.2 Effect of 24a on mitochondrial, cellular ROS, and oxidative stress in the Drosophila model of AD

The detection of mitochondrial superoxide involves the utilization of MitoSOX Red, a specialized indicator for mitochondria-derived superoxide. The positive charge carried by the triphenylphosphonium group facilitates its penetration through the phospholipid bilayer, enabling effective accumulation in the mitochondrial matrix. The hydroethidine component of MitoSOX Red plays a crucial role in distinguishing the fluorescent signal generated explicitly by superoxide-mediated oxidative products from other non-specific signals. In our observations, untreated third instar larval eye imaginal discs from the AD model exhibited a

4.75-fold increase in superoxide compared to the control, as depicted in **Figure 4.32** (A, B), and (a, b). However, upon treatment of AD larvae with **24a** at 0.05 mg (127.18 µM)/ml, superoxide levels became comparable to the control, as illustrated in **Figure 4.32** (A, C), and (a, c), showing a reduction to 1.18-fold. When concentrations of 0.1 mg (254.36 µM)/ml of **24a** were administered, the superoxide levels were found to be 1.57-fold higher, as depicted in **Figure 4.32** (A, D and a, d), within the AD larval eye imaginal discs compare to control. In contrast, standard drug **DPZ** treatment resulted in superoxide levels similar to the power, as seen in **Figure 4.32** (A, E and a, e). These findings suggest that **24a** exhibits greater efficacy at lower doses (0.05 mg/ml) than at higher doses (0.1 mg/ml) in mitigating excessive mitochondrial superoxide in the AD Drosophila model.

2′,7′-Dichlorodihydrofluorescein diacetate (H2DCFDA) stands out as a widely employed probe for assessing cellular hydrogen peroxide (H_2O_2) levels[185]. This cell-permeable compound permeates cell membranes and undergoes deacetylation catalyzed by intracellular esterases, forming 2′,7′-dichlorodihydrofluorescein (H2DCF). Upon exposure to reactive oxygen species (ROS), H2DCF undergoes rapid oxidation, producing 2′,7′-dichlorofluorescein (DCF). DCF exhibits heightened fluorescence with excitation and emission wavelengths of 498 and 522 nm, respectively. We also used H2DCFDA to assess total cellular ROS levels in OregonR+ and AD larval eye imaginal discs treated with **24a** and **DPZ**, comparing them with untreated AD larval eye imaginal discs. Our findings revealed a 4.34-fold increase in cellular ROS in untreated AD larval eye imaginal discs compared to the control, as illustrated in **Figure 4.33** (**A**, **B**) and (**a**, **b**). Upon treatment with **24a** at concentrations of 0.05 mg (127.18 µM)/ml and 0.1 mg (254.36 µM)/ml, we observed a significant reduction in excessive cellular ROS to 1.18-fold and 1.57-fold, respectively, in comparison to the control, as shown in **Figure 4.33**

(**A**, **C**, **D**) and (**a**, **c**, **d**) in the treated AD larvae group. In contrast, the standard drug **DPZ**, at a concentration of 100 µM, reduced cellular ROS levels equivalent to the control group, as depicted in **Figure 4.33** (**A**, **E**) and (**a**, **e**). These results strongly indicate that **24a**, particularly at the lower 0.05 mg/ml concentration, exhibits greater efficacy in protecting against oxidative stress in the AD Drosophila model. The significant reduction in mitochondrial ROS as well as cellular ROS levels suggests that **24a** may hold promise as a potential therapeutic agent for mitigating oxidative stress associated with AD.

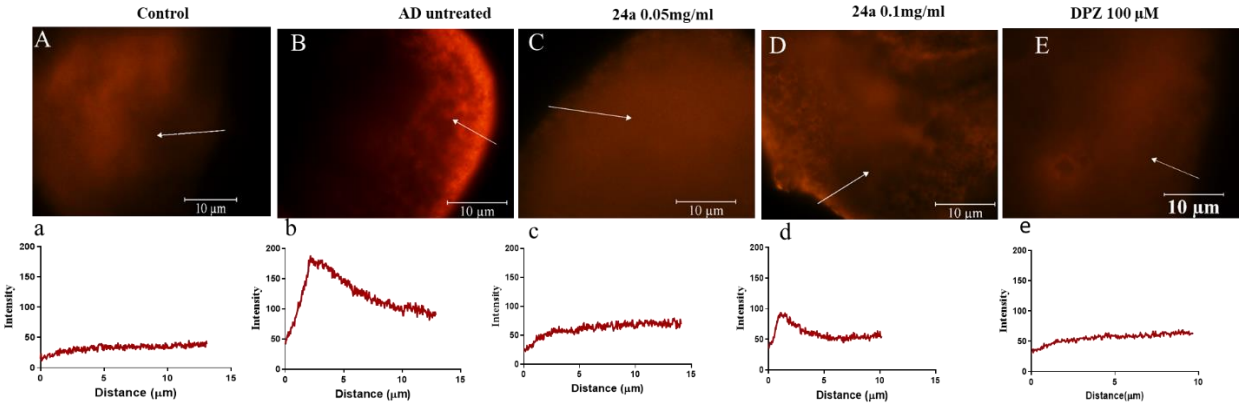

Figure 4.32: Mitochondrial superoxide (ROS) level measurement in Oregon+ and Aβ42 expressing eye imaginal discs of Drosophila.Fluorescent images of 3rd instar larval eye discs stained with MitoSOX Red. A) Control, **B**) AD untreated, **C**) AD treated with **24a** 0.05 mg/ml, **D)** AD treated with **24a** 0.1 mg/ml, e) **DPZ** 100 μM. The line graph represents the fluorescence intensity of MitoSOX Red in each group's 3rd instar larval eye imaginal discs. The Y-axis represents intensity, while the X-axis indicates distance (µm).

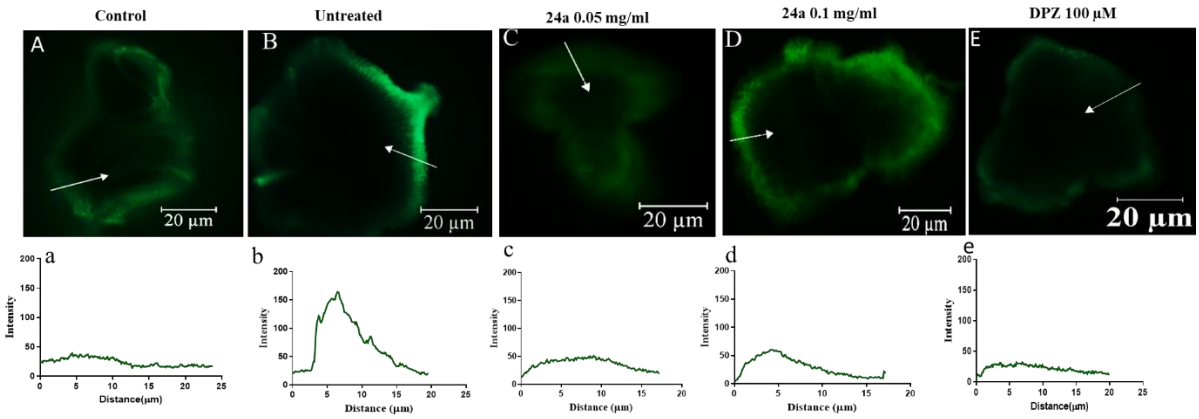

Figure 4.33: Measurement of total cellular ROS level in OregonR+ and Aβ42 expressing eye imaginal discs of Drosophila. Fluorescent images of 3rd instar larval eye discs stained with H2DCFDA. A) Control, B) AD untreated, C) AD treated with **24a** 0.05 mg/ml, D) AD treated with **24a** 0.1 mg/ml, E) **DPZ** 100 µM. iiA line graph illustrating the fluorescence intensity of H2DCFDA in the eye imaginal discs of 3rd instar larvae for each experimental group. The line graphs, generated using NIS-Elements BR 4.3 software, display the intensity on the Y-axis and distance (µm) on the X-axis, representing the *in situ* ROS produced in the eye imaginal discs of the control group, untreated group, **24a**-treated group, and **DPZ**-treated AD model of Drosophila.

4.6.12 *In-vivo* evaluation of 24a

I carried out animal experiments at the Department of Pharmaceutical Engineering and Technology, IIT (BHU), under Dr. Prashanta Kumar Nayak's guidance, with Himanshu Verma's help.

4.6.12.1 Acute toxicity studies of 24a

To evaluate the acute toxicity of **24a**, we use healthy male Swiss albino mice (25-30g), following the OECD guidelines and our previous publication for determining acute toxicity

[150]. The mice were administered compound **24a** at doses up to 550 mg/kg and kept under observation for 14 days for any symptoms of toxicity, such as changes in water or food consumption, hair loss, weight loss (**Figure 4.34**), abnormal behavior, and death. However, no such symptoms were observed. On the 14th day, all mice were sacrificed. These results indicate compound **24a** did not cause acute toxicity in the mice at the tested dose.

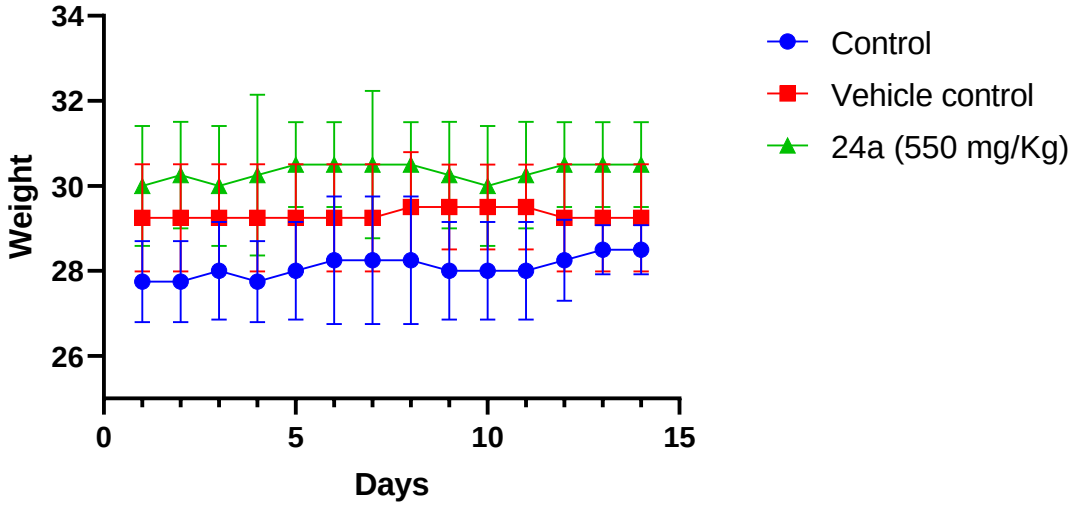

Figure 4.34: The mean ± SD of body weights for control, vehicle control, and compound **24a** (at 550 mg/kg) treated groups with a sample size of n = 6 mice per group. Statistical analysis involved a two-way ANOVA and the Bonferroni test, $P > 0.05$.

4.6.12.2 Determination of *in-vivo* efficacy 24a to ameliorate spatial and learning impairment in scopolamine-induce amnesia in an animal model.

To evaluate the *in-vivo* anti-cholinesterase (anti-ChE) activity of the most effective compound **24a** in the series, the scopolamine-induced amnesia model was utilized. This model, well-

established in behavioral pharmacology, is widely recognized for assessing the inhibitory effects of drug candidates on cholinesterase (ChE), an enzyme crucial for memory and learning processes. The administration of scopolamine selectively inhibits muscarinic cholinergic receptors, leading to a significant deterioration in cognitive function. The Y-maze experiment was utilized to assess the potential of **24a** to reverse the spatial memory impairment induced by scopolamine. Healthy male Swiss albino mice were administered compound **24a** at doses of 1 mg, 5 mg/kg (IP), and **DPZ** 1 mg/kg (IP) for seven days, with body weights analyzed (**Figure 4.35 A**). On the 7th day, spatial working memory was evaluated through the Y-maze experiment following the administration of scopolamine hydrochloride. Mice received treatment with either **24a** or **DPZ** 30 minutes before scopolamine administration, and spontaneous alterations were assessed after 15 minutes of scopolamine administration. The scopolamine-treated group induced amnesia and exhibited a noteworthy decline in spontaneous alternation and arm entries. In contrast, **24a** and **DPZ** demonstrated increased spontaneous alternations (**Figure 4.35 B**), suggesting their potential to alleviate amnesia. The enhanced spontaneous alternation of **24a**, likely mediated by its anti-AChE effect, indicates its efficacy as a cholinesterase inhibitor and that it can cross the blood-brain barrier. The findings suggest that **24a** holds considerable promise in enhancing spatial and immediate memory in mice within the scopolamine-induced amnesia model. The total number of arm entries in the Y-maze experiment did not changed among the different treatments group (**Figure 4.35 C**).

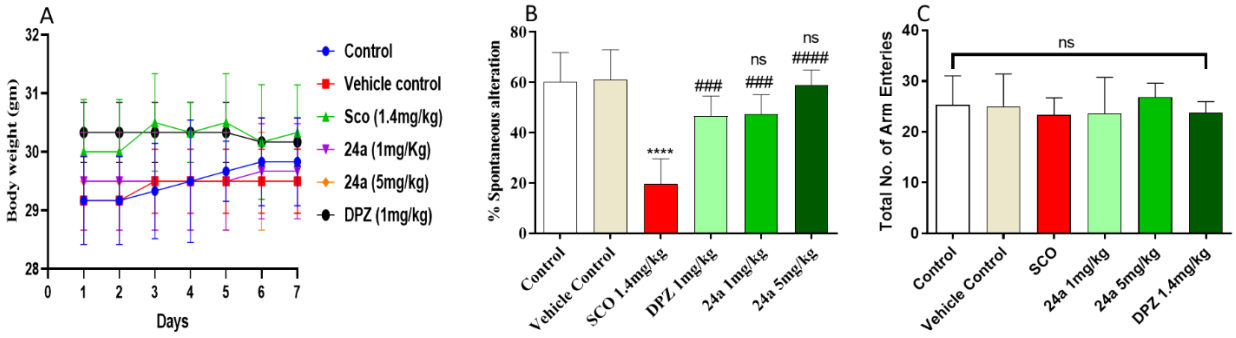

Figure 4.35: Scopolamine-induced amnesia and memory impairment in mice. A) Mean body weight of each group during 7 days of drug treatment. B) The impact of compound **24a** on scopolamine-induced memory impairment was assessed using the Y-maze test. **24a** (1 and 5 mg/kg, ip) and **DPZ** (1 mg/kg, ip) were administered in mice for 7 days. On the 7th day, after 30 minutes of **24a** and **DPZ** administration, the mice received scopolamine (1.4 mg/kg, ip) and, after 15 minutes, were subjected to a Y-maze test. % spontaneous alteration was calculated. C) The total number of arm entries in the Y-maze experiment. The data are presented as the mean ± SEM (n = 6). Statistical significance is denoted as ***$p < 0.001$ compared to the control and vehicle control, ###$p < 0.001$ and ####$p < 0.0001$ compared to scopolamine, and $^{ns}p > 0.05$ compared to **DPZ**. ns indicates non-significant differences. Data were analyzed using one-way ANOVA followed by Tukey's multiple comparisons.

4.6.13 *Ex-Vivo* and biochemical Analysis of neurotransmitters.

In further experimentation, the effect of **24a** on the AChE and BChE levels of the brain was estimated in mice using Ellman's method, as described in our previous report. Scopolamine treatment significantly elevated AChE and BChE levels compared to the vehicle-treated control group. However, the elevated levels of AChE and BChE were attenuated considerably by compound **24a** at a 5 mg/kg ipl dose. The lead compounds showed similar activity as a reference drug, donepezil, but at a slightly higher dose. The result revealed that both the

compounds attenuate the elevated concentration of AChE and BChE efficiently and impart their pharmacological effect against the cholinesterase enzyme (**Figure 4.36 A** and **B**). To further understand the anti-amnesic mechanism of compound **24a**, brain levels of malondialdehyde (MDA), a byproduct of lipid peroxidation, were assessed after completion of the Y-maze test using a method from a previous study. Scopolamine treatment significantly increased MDA levels compared to the vehicle-treated control group. However, administration of compound **24a** effectively reduced MDA levels in amnesic mice. CAT, a key antioxidant defense system, is crucial in breaking down hydrogen peroxide into water and oxygen, countering reactive oxygen species (ROS) and oxidative stress (**Figure 4.36 C**). Superoxide dismutase (SOD), an essential antioxidant enzyme defending the brain against oxidative stress, exhibited significantly reduced levels in scopolamine-treated animals compared to control and vehicle-treated groups. In contrast, lead molecule **24a** demonstrated a capacity to restore diminished SOD levels in scopolamine-treated animals effectively (**Figure 4.36 D**). This implies a protective influence on the brain, potentially counteracting scopolamine-induced memory impairment. Treatment with lead molecule **24a** emerges as a promising approach to elevate SOD levels in the brains of scopolamine-treated animals, offering protection against the detrimental effects of this drug on memory and cognitive function. Scopolamine treatment decreased CAT levels in treated animals compared to the vehicle and control groups, indicating increased oxidative stress. Conversely, treatment with **24a** significantly raised CAT levels in the brains of treated animals (**Figure 4.36 E**). This observation suggests these compounds possess antioxidant capabilities, mitigating oxidative stress and shielding cells from damage.

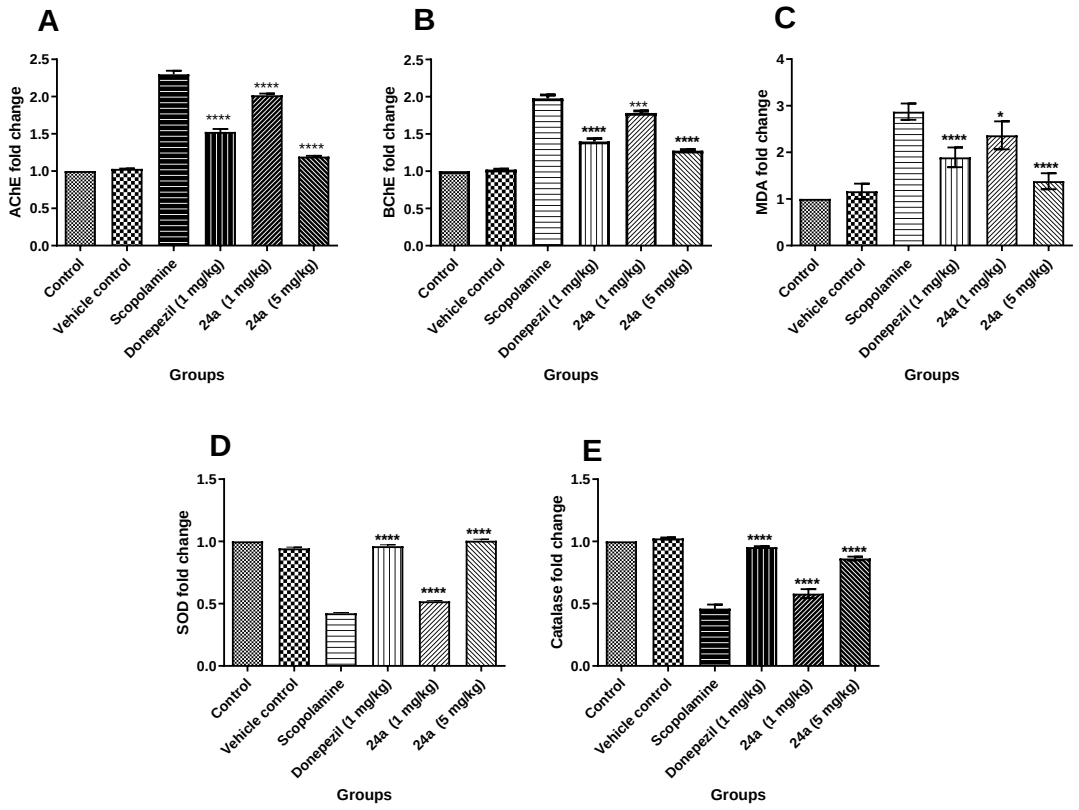

Figure 4.36: The impact of compound **24a**, donepezil (**DPZ**), and scopolamine on various neurochemical parameters, such as AChE, BChE, MDA, SOD, and catalase CAT levels. A) **24a** effectively reduces elevated AChE levels, suggesting its role in regulating cholinergic function. B) **24a** significantly reduces BChE levels induced by scopolamine, inhibiting BChE activity. C) **24a** enhances SOD activity, demonstrating its antioxidant effects. D) Compound **24a** reduces MDA levels, indicating a mitigating effect on oxidative damage. E) **24a** influences CAT activity, providing a countermeasure against oxidative stress. Data are expressed as mean ± SEM (n = 6), ****p < 0.0001, ***p = 0.0004, *p = 0.0107, vs. scopolamine group (One-way ANOVA followed by Tukey's multiple comparison test)

.